LUDWIG-MAXIMILIANS-UNIVERSITÄT MÜNCHEN

BACHELOR THESIS

Finite Element Analysis and Fabrication of a Bow-tie Antenna for Terahertz Detection

Finite Elemente Analyse und Fabrikation einer Schmetterlingsantenne für Terahertz Detektion

Chair of Experimental Solid State Physics – Quantum Materials[†]

Author

Carl A. Hudeczek
`carl.hudeczek@campus.lmu.de`
LMU Munich

Supervisors

Prof. Dr. Dmitri K. Efetov   Giorgio di Battista
`dmitri.efetov@lmu.de`   `giorgio.dibattista@lmu.de`
LMU Munich   LMU Munich

Munich, July 22, 2024

[†]`https://quantummatter.physik.lmu.de`

Abstract

Terahertz detectors utilizing the unique band structure properties of moiré materials rely on the use of antennas to funnel the radiation efficiently into the sensing element. Those antennas are required to have a high effective area and need to be impedance matched to the sensing element to maximize the power delivered by the incident radiation. For this thesis, a MATBG-based detector is considered with the goal of establishing guidelines for the design and fabrication of a bow-tie antenna for this exact purpose. By finite element simulations of a simplified physical model and interpolation of the acquired data, a parameter configuration for an antenna with a desired resonance frequency of $0.5\,\mathrm{THz}$ was predicted. The finalized antenna design was fabricated on silicon as a substrate through photolithography and subsequent thin-film deposition of gold via evaporation.

Contents

CONTENTS

1 Introduction

Terahertz radiation promises new technological advancements making it of high interest to the subject of research for practical applications such as quantum sensing, biomedical imaging, and communications technology. [1]

Until recently, technology and scientific progression utilizing terahertz radiation was limited due to a lack of mainstream transmitter and detector technology. The terahertz spectrum is at the boundary between the well-developed fields of high-frequency electronics and infrared optics, which is, due to the lack of available technology, commonly referred to as the terahertz gap. Traditional electronic devices are too slow to utilize alternating voltages and currents in the terahertz regime, whereas a lack of suitable semiconductor materials with band gaps that are smaller than the energy of a terahertz photon prevents progression towards the terahertz gap from the field of photonics. A promising pathway to bridge the technological gap of photonics and optoelectronics in the terahertz range is presented by the use of moiré materials, which are constituted by two-dimensional layers rotated with respect to each other at specific twist angles. Such rotation, resulting in a change of periodicity of a crystal, can be used to engineer the band structure to obtain ultra-low carrier density superconducting phases at low temperatures, which could enable terahertz detection. [2–5]

The unique band structure of MATBG opens up new means to detect terahertz radiation and possibly allows to overcome the terahertz gap from an optoelectronical approach. To efficiently funnel the terahertz radiation into the sensing element, antennas become a requirement, which absorb incident radiation by orders of magnitude better than any standalone graphene sensing element up to date. A possible choice of such an antenna is the bow-tie antenna, or derivatives thereof, which excel in their simple design and ability to efficiently couple the radiation into the feed compared to other antenna designs. [1, 3–8]

The sensing geometry and configuration of such a terahertz detection setup is shown in Fig. 1.1.

(a) antenna configuration

(b) sensing element configuration
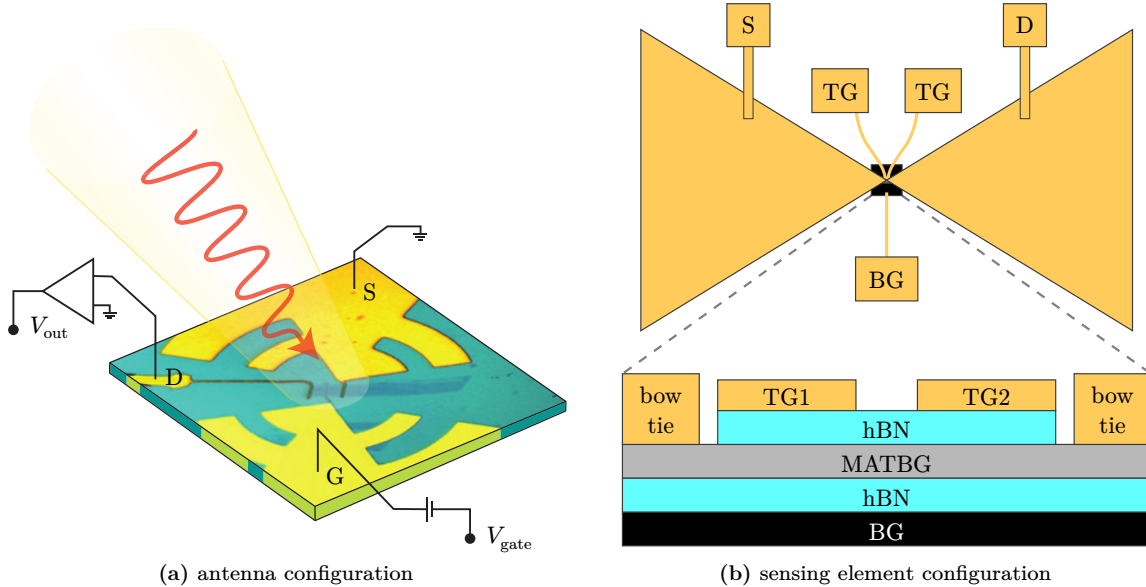
Figure 1.1: Nomenclature: source S, gate G, drain D, top gate TG, back gate BG, magic-angle twisted bilayer graphene MATBG, hexagonal boron nitride hBN. (a) Schematic of a circular-toothed log-periodic antenna connected to a graphene gate acting as the sensing element. The incident terahertz radiation is captured by the antenna and funneled into the feed. Adapted from [6, fig. 1c]. (b) Schematic of the gate structure, consisting of multiple stacked two-dimensional material layers. Adapted from [8, fig. 1 left].

This thesis aims to design the most suitable antenna for such a setup. The experiment in question

relies on a MATBG-based sensing element in a geometrical Hall bar configuration and a monochromatic tunable terahertz source which are placed inside a dilution refrigerator and cooled down to temperatures of few kelvins. For this thesis a bow-tie-shaped antenna is considered with the goal of optimizing the antenna's funneling of the incident electric field according to the experimental parameters. This objective is achieved by employing the finite element method for a simulation model of the real experimental setup to obtain helpful insights for the design of the most adequate antenna geometry.

Two criteria are of particular concern when attempting to find the antenna's most optimal configuration. Firstly, the radiation absorbed by the antenna should be maximized as much as possible, considering the low output power of the tunable gallium arsenide photomixer that is used as a terahertz source for the experimental setup of the to-be-fabricated bow-tie antenna, and secondly, the antenna should be impedance matched to the graphene element as close as possible due to the reasons outlined in Sec. 2. Due to the two-dimensional geometry of the sensing element, one-dimensional contacts are formed between the antenna and multilevel stack. The contact impedance between antenna and graphene depends on various factors, where the contact impedance of such a sensing element can under certain circumstances be as high as $10\,\mathrm{k\Omega}$, prompting the need to take reflection losses at the antenna feed into consideration. [5–7, 9–11]

Throughout this thesis, design guidelines for a bow-tie antenna in a similar experimental configuration as in Fig. 1.1 are established via finite element simulations in Sec. 3 and Sec. 4. The resonance behavior of the bow-tie parameters is studied for frequencies up to $2\,\mathrm{THz}$ with a target resonance frequency of $0.5\,\mathrm{THz}$, due to the emission spectrum of the utilized photomixer with a functional frequency interval of roughly $0.1\,\mathrm{THz}$ to $2\,\mathrm{THz}$. At last, the fabrication process of the antenna via photolithography on silicon as a substrate is outlined in Sec. 5.

2 Theoretical Fundamentals

This section covers a brief introduction to the theoretical fundamentals of the required physics, which in turn motivates both the utilized methods for setting up the simulation model and the general idea behind the data analysis methodologies.

2.1 Maxwell's Equations

Maxwell's equations are a set of differential equations yielding a full description of the electric ($\mathbf{E}$) and magnetic ($\mathbf{H}$) fields generated by electric charges (with charge density ρ) and electric currents (with current density $\mathbf{j}$). They are generally well understood, albeit not analytically solvable in general scenarios. One of the most common formulations of Maxwell's equations in their differential form (in this case specifically the so-called macroscopic equations) consists of 4 coupled partial differential equations [12, eq. 3-1]:

$$\boldsymbol{\nabla} \cdot \mathbf{D} = \rho \tag{2.1}$$

$$\boldsymbol{\nabla} \times \mathbf{E} = -\frac{\partial \mathbf{B}}{\partial t} \tag{2.3}$$

$$\boldsymbol{\nabla} \cdot \mathbf{B} = 0 \tag{2.2}$$

$$\boldsymbol{\nabla} \times \mathbf{H} = \mathbf{j} + \frac{\partial \mathbf{D}}{\partial t} \tag{2.4}$$

with the three constitutive relations [12, eq. 3-3]:

$$\text{Electric displacement field} \quad \mathbf{D} = \varepsilon_0 \mathbf{E} + \mathbf{P} \tag{2.5}$$

$$\text{Magnetic flux density} \quad \mathbf{B} = \mu_0 (\mathbf{H} + \mathbf{M}) \tag{2.6}$$

$$\text{Current density} \quad \mathbf{j} = \sigma \mathbf{E} \tag{2.7}$$

where $\mathbf{P}$ is the dipole moment and $\mathbf{M}$ the magnetization, both quantities being material dependent properties. The constant ε_0 is the permittivity, μ_0 the permeability of vacuum, and σ the material's conductivity[1]. In linear and isotropic media, $\mathbf{P}$ and $\mathbf{M}$ are directly proportional to the incident $\mathbf{E}$ and $\mathbf{H}$ fields respectively, simplifying the respective expressions to [12, p. 77][13, eqs. 3.8(5)–3.8(7)]:

$$\mathbf{D} = \varepsilon_0 \varepsilon_{\mathrm{r}} \mathbf{E} = \varepsilon \mathbf{E} \tag{2.8}$$

$$\mathbf{B} = \mu_0 \mu_{\mathrm{r}} \mathbf{H} = \mu \mathbf{H} \tag{2.9}$$

Which in turn simplifies Maxwell's equations to:

$$\boldsymbol{\nabla} \cdot \mathbf{E} = \frac{\rho}{\varepsilon} \tag{2.10}$$

$$\boldsymbol{\nabla} \times \mathbf{E} = -\frac{\partial \mathbf{B}}{\partial t} \tag{2.12}$$

$$\boldsymbol{\nabla} \cdot \mathbf{B} = 0 \tag{2.11}$$

$$\boldsymbol{\nabla} \times \mathbf{B} = \mu \mathbf{j} + \varepsilon \mu \frac{\partial \mathbf{E}}{\partial t} \tag{2.13}$$

They are the fundamental equations describing the behavior of electromagnetic fields, their interaction with matter, and therefore ultimately also the radiative behavior of antennas. For the task of modeling a functional antenna, there are two analytical solutions of particular interest.

2.1.1 Homogeneous Plane Wave Solution

Under the assumption of a charge and current free environment, it is possible to rewrite Maxwell's equations to obtain the homogeneous wave equations for electromagnetic fields [14, p. 8]:

---

[1]Additionally, ε and μ denote, respectively, the permittivity and permeability of an arbitrary linear and isotropic material, with ε_{r} and μ_{r} being the relative values, with their relationship as given in Eq. (2.8) and Eq. (2.9).

$$\frac{n^2}{c^2}\frac{\partial^2 \mathbf{E}}{\partial t^2} - \boldsymbol{\nabla}^2 \mathbf{E} = 0 \qquad (2.14) \qquad\qquad \frac{n^2}{c^2}\frac{\partial^2 \mathbf{B}}{\partial t^2} - \boldsymbol{\nabla}^2 \mathbf{B} = 0 \qquad (2.15)$$

The plane wave solution in complex representation equates to the following expressions, with the sign convention as used in *COMSOL* [12, p. 84][14, p. 10]:

$$\mathbf{E}(t,\mathbf{x}) = \mathbf{E_0}e^{i(\omega t - n\mathbf{k}\cdot\mathbf{x})} \qquad (2.16) \qquad\qquad \mathbf{B}(t,\mathbf{x}) = \mathbf{B_0}e^{i(\omega t - n\mathbf{k}\cdot\mathbf{x})} \qquad (2.17)$$

This solution proves to be useful when modeling the antenna via *COMSOL* to specify the incident fields and to calculate various other properties of interest. A comprehensive and detailed derivation of the results and related physical quantities is given in Apdx. A.1.

2.1.2 Jefimenko's Equations

Jefimenko's equations are a generalized solution to Maxwell's equations. It is possible to calculate the full electromagnetic field for any given charge and current distribution over spacetime, as the calculations take the spatial time retardation of the fields into account, since the electromagnetic fields cannot propagate faster than the speed of light, and thus cause and effect are not instantaneous, but rather delayed in spacetime.

The solution is valid under the assumption that the resulting fields do not contribute to or interact with any new or preexisting currents and charges. The derivation is complicated and lengthy, so only the general idea will be outlined and the solution given.

From Maxwell's equations, it is possible to introduce two new potentials. One is called the scalar potential Φ, the other one the vector potential $\mathbf{A}$. Their mathematical description is derived from Maxwell equation Eq. (2.11) and Eq. (2.12) in combination with the vector identity Eq. (A.29). In SI units, they relate to the electric and magnetic fields as follows [15, eqs. 6.7, 6.9]:

$$\mathbf{E}(t,\mathbf{x}) = -\boldsymbol{\nabla}\Phi(t,\mathbf{x}) - \frac{\partial \mathbf{A}(t,\mathbf{x})}{\partial t} \qquad (2.18) \qquad\qquad \mathbf{B}(t,\mathbf{x}) = \boldsymbol{\nabla}\times\mathbf{A}(t,\mathbf{x}) \qquad (2.19)$$

The next step is to obtain an expression for these two potentials at any given point in spacetime, the so-called retarded potentials [15, eq. 6.48]:

$$\Phi(t,\mathbf{x}) = \frac{1}{4\pi\varepsilon_0}\int \mathrm{d}^3\mathbf{x}' \frac{1}{R}\left[\rho(t',\mathbf{x}')\right]_{\mathrm{ret}} \qquad (2.20)$$

$$\mathbf{A}(t,\mathbf{x}) = \frac{\mu_0}{4\pi}\int \mathrm{d}^3\mathbf{x}' \frac{1}{R}\left[\mathbf{J}(t',\mathbf{x}')\right]_{\mathrm{ret}} \qquad (2.21)$$

Now all that is left to do is to apply the definition for the electromagnetic fields by inserting the introduced potentials in Eq. (2.20) and Eq. (2.21) into their definition from Eq. (2.18) and Eq. (2.19) to obtain Jefimenko's equations[2] [15, eqs. 6.51, 6.52]:

$$\mathbf{E}(t,\mathbf{x}) = \frac{1}{4\pi\varepsilon_0}\int \mathrm{d}^3\mathbf{x}' \frac{1}{R}\left[-\boldsymbol{\nabla}'\rho(t',\mathbf{x}') - \frac{1}{c^2}\frac{\partial \mathbf{J}(t',\mathbf{x}')}{\partial t'}\right]_{\mathrm{ret}} \qquad (2.22)$$

$$\mathbf{B}(t,\mathbf{x}) = \frac{\mu_0}{4\pi}\int \mathrm{d}^3\mathbf{x}' \frac{1}{R}\left[\boldsymbol{\nabla}'\times\mathbf{J}(t',\mathbf{x}')\right]_{\mathrm{ret}} \qquad (2.23)$$

Hereby, some of the used expressions evaluate explicitly to [15, eqs. 6.53, 6.54]:

---

[2]In these calculations $[\ ]_{\mathrm{ret}}$ indicates that the time t' must be evaluated at the retarded time $t' = t - R/c$. Per this definition extra care is required, as the effect of $\boldsymbol{\nabla}'$ varies whether the symbol is inside or outside the $[\ ]_{\mathrm{ret}}$ brackets. If inside the brackets, $\boldsymbol{\nabla}'$ denotes the spatial gradient with regard to $\mathbf{x}'$ with t' fixed, if outside, $\boldsymbol{\nabla}'$ denotes the spatial gradient with regard to $\mathbf{x}$ with t' and $\mathbf{x}'$ fixed. [15, pp. 246–248]

$$\mathbf{R} = \mathbf{x} - \mathbf{x}' \qquad (2.24) \qquad\qquad R = |\mathbf{R}| \qquad (2.25) \qquad\qquad \hat{\mathbf{R}} = \frac{\mathbf{R}}{R} \qquad (2.26)$$

$$\boldsymbol{\nabla}'\rho(t', \mathbf{x}') = \boldsymbol{\nabla}'\left[\rho(t', \mathbf{x}')\right]_{\mathrm{ret}} - \frac{\hat{\mathbf{R}}}{c}\left[\frac{\partial \rho(t', \mathbf{x}')}{\partial t'}\right]_{\mathrm{ret}} \qquad (2.27)$$

$$\left[\boldsymbol{\nabla}' \times \mathbf{J}(t', \mathbf{x}')\right]_{\mathrm{ret}} = \boldsymbol{\nabla}' \times \left[\mathbf{J}(t', \mathbf{x}')\right]_{\mathrm{ret}} + \frac{1}{c}\left[\frac{\partial \mathbf{J}(t', \mathbf{x}')}{\partial t'}\right]_{\mathrm{ret}} \times \hat{\mathbf{R}} \qquad (2.28)$$

2.2 RF Engineering Fundamentals

Moving away from Maxwell's equations, there are important considerations that have to be made regarding the circuit configuration of antennas. Maxwell's equations describe the radiative properties of any antenna in detail, yet their behavior in an electrical circuit remains to be described. A measure of quality is necessary to compare the performance of different antenna designs. There are many quantities describing certain aspects of the antenna, but for this thesis only a handful of them is needed to deduce an antennas suitability for the experiment of interest. A short introduction to transmission lines and linear networks is necessary to understand the concept of scattering parameters and why they prove to be useful to determine the antennas adequacy for the intended use case.

2.2.1 Transmission Lines

When alternating voltages and currents are used within an electrical circuit, wave-like properties have to be accounted for when electrical connections between different elements of the circuit are long enough. If the value of a voltage or current signal at a fixed time varies along the position of an electric connection, the circuit cannot be modeled as a regular RCL circuit and transmission line effects have to be considered. A commonly used threshold to determine if transmission line effects are significant is whether the length of any interconnection in the circuit is longer than (depending on the application) $\lambda/20$ to $\lambda/5$ of the highest frequency component of the signal. For example, applying the criterion to a signal with a frequency of 1 THz (and a corresponding free-space wavelength of $\sim 300\,\mu\mathrm{m}$) results in a significant interconnect length between roughly $15\,\mu\mathrm{m}$ to $60\,\mu\mathrm{m}$. On a transmission line, voltage and current are not only dependent on the time, but also on the position. [16, sec. 2.1]

For high enough frequencies, this makes it difficult to define something like a shared ground point for all the electrical components in a circuit, as the ground may differ significantly from one location to the other. Transmission lines are therefore preferably realized as cables with two conductors instead of one. [17, sec. 2]

Visualized in Fig. 2.1 and independent of the geometry, any transmission line can be modeled by four specific parameters; the series resistance R, the series inductance L, the shunt conductance G, and the shunt capacitance C. The units of these parameters are specified per unit length. The most dominant contributions are mostly due to the characteristic inductance and capacitance. If R and G are equal to 0, the transmission line is called lossless. These properties come in handy when defining the characteristic impedance of the transmission lines [16, sec. 2.2.1].
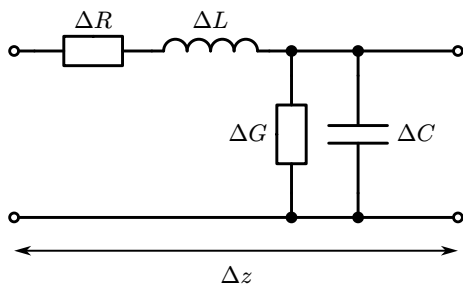
Figure 2.1: RLGC model of a small transmission line segment of length Δz. The lumped elements impose boundary conditions for the voltage and current at the connection nodes of the segment. Adapted from [16, fig. 2-5].

By applying Kirchhoff's laws to the model, one obtains the transmission line equations[3] [16, eqs. 2.4, 2.5]:

$$\frac{\partial V(t,z)}{\partial t} = -RI(t,z) - L\frac{\partial I(t,z)}{\partial t} \qquad (2.29) \qquad \frac{\partial I(t,z)}{\partial t} = -GV(t,z) - C\frac{\partial V(t,z)}{\partial t} \qquad (2.30)$$

For sinusoidal voltages and currents of the given form, the solutions for $V(z)$ and $I(z)$ are as follows [16, eqs. 2.11, 2.12]:

$$V(t,z) = \Re\{V(z)e^{i\omega t}\} \qquad (2.31) \qquad\qquad I(t,z) = \Re\{I(z)e^{i\omega t}\} \qquad (2.33)$$

$$V(z) = \underbrace{V_0^+ e^{-\gamma z}}_{=V^+(z)} + \underbrace{V_0^- e^{+\gamma z}}_{=V^-(z)} \qquad (2.32) \qquad\qquad I(z) = \underbrace{I_0^+ e^{-\gamma z}}_{=I^+(z)} + \underbrace{I_0^- e^{+\gamma z}}_{=I^-(z)} \qquad (2.34)$$

where γ is the propagation constant, α the attenuation coefficient, and β the phase-change coefficient [16, eq. 2.10]:

$$\gamma = \alpha + i\beta = \sqrt{(R + i\omega L)(G + i\omega C)} \qquad (2.35)$$

The obtained solutions for $V(t,z)$ and $I(t,z)$ consist of one forward-traveling wave in $+z$ direction ($V^+(z)$ and $I^+(z)$), and one backward-traveling wave in $-z$ direction ($V^-(z)$ and $I^-(z)$) respectively.

With these solutions, it is now possible to define the characteristic impedance Z_0 of the transmission line, allowing one to relate the forward- and backward-traveling components of voltage and current [16, eq. 2.15]:

$$Z_0 = \frac{V_0^+}{I_0^+} = -\frac{V_0^-}{I_0^-} = \sqrt{\frac{R + i\omega L}{G + i\omega C}} \qquad (2.36)$$

From now on, only lossless transmission lines shall be considered. In the scenario that the transmission line is terminated at a load with impedance Z_L, back reflection occurs, if $Z_L \neq Z_0$. This is the case as Z_L imposes a condition on the voltage V_L and current I_L at the interface between the transmission line and load [16, eq. 2.56]:

$$\frac{V_L}{I_L} = \frac{V(z=0)}{I(z=0)} = Z_0\frac{V_0^+ + V_0^-}{V_0^+ - V_0^-} \qquad (2.37)$$

This equation can now be rearranged to obtain the ratio between the reflected and incident voltage, and thus define the so-called voltage reflection coefficient Γ^V (or just the wave reflection coefficient Γ), and concurrently also the current reflection coefficient Γ^I at the load [16, eqs. 2.59, 2.63]:

$$\Gamma \equiv \Gamma^V = \frac{V_0^-}{V_0^+} = \frac{Z_L - Z_0}{Z_L + Z_0} \qquad (2.38) \qquad\qquad \Gamma^I = \frac{I_0^-}{I_0^+} = \frac{Z_0 - Z_L}{Z_0 + Z_L} = -\Gamma^V \qquad (2.39)$$

Hereby, Γ can be any complex number with $|\Gamma| \leq 1$, with the absolute value governing the magnitude of the reflected wave and the argument the phase shift between the incident and reflected wave. The important takeaway from this is that at every impedance mismatched interface reflection occurs (see Fig. 2.2).

Reflections are important to consider when describing the power flow and return loss at such interfaces. The time-averaged power of the incident (P^+) and reflected wave (P^-) can be calculated as follows, and via Eq. (2.36) and Eq. (2.38) also simplified to [16, eqs. 2.163, 2.164]:

$$\langle P^+\rangle_T = \frac{1}{2}\left|\frac{(V_0^+)^2}{Z_0}\right| \qquad (2.40) \qquad \langle P^-\rangle_T = \frac{1}{2}\left|\frac{(V_0^-)^2}{Z_0}\right| = \frac{|\Gamma|^2}{2}\left|\frac{(V_0^+)^2}{Z_0}\right| = |\Gamma|^2\langle P^+\rangle_T \qquad (2.41)$$

---

[3]In engineering, it is common to use complex valued (so-called phasors) $V(z)$ and $I(z)$ for calculations with sinusoidal alternating voltages and currents. The benefit of using phasors is that voltage and current are solely defined by their spatial position and phase shift, as the time behavior (which is sinusoidal, and therefore in complex representation $e^{i\omega t}$) is well-known. Usually, the voltage and currents are denoted as $v(t,z) = \Re\{V(z)e^{j\omega t}\}$ and $i(t,z) = \Re\{I(z)e^{j\omega t}\}$, but to prevent a collision with the symbol for the imaginary unit, engineers resort to naming the imaginary unit j instead of i as customary for mathematicians and physicists. In the thesis, this shall be avoided by defining $v(t,z) \equiv V(t,z)$ and $i(t,z) \equiv I(t,z)$ (with the definitions of $V(z)$ and $I(z)$ being equivalent in both conventions).
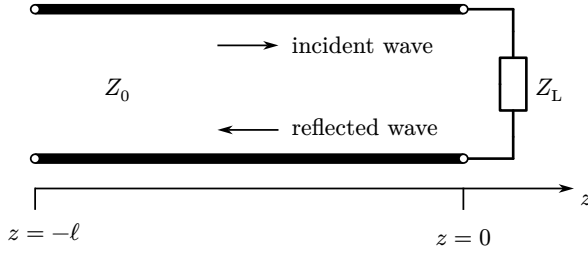
Figure 2.2: Terminated transmission line of length ℓ with load impedance Z_{L}. If there is an impedance mismatch, reflection occurs. Any effects related to the transmission line length are not considered throughout this thesis. Adapted from [17, fig. 2-12].

Consequently, the actual power delivered to the load is [18, eq. 2.165]:

$$\langle P_{\mathrm{L}} \rangle_T = \langle P^+ \rangle_T - \langle P^- \rangle_T = \langle P^+ \rangle_T (1 - |\Gamma|^2) \tag{2.42}$$

The wave reflection coefficient is therefore an excellent measure of quality for antennas to quantify their efficiency at absorbing incident power of electromagnetic waves. Even though the sensing element and antenna are not connected to any transmission lines, the concept should still prove to be very useful, as the interface between the sensing element and antenna is heavily impedance mismatched. Optimizing the wave reflection coefficient could therefore be a good approach in designing the most optimal antenna for the desired experimental configuration. [6, 7, 9]

2.2.2 *N*-port networks

The concept of reflection parameters as introduced in Sec. 2.2.1 was restricted to transmission lines only, and moreover to just one interface at a time. It is, however, necessary to generalize this newly introduced paradigm when dealing with distributed circuits, as at high frequencies a circuit can no longer be localized due to the wave-like effects and because they can consist of more than just one input port. It is still not possible to define a universal ground. For this thesis, the concept of *N*-port networks is not needed in its fully generalized version, as a one-port network will suffice fully to describe the experimental setup with the antenna coupled to the sensing element.

For now, it is sufficient to think of a *N*-port network as a black box with *N* in- and outputs (called ports) as in Fig. 2.3, that relate to each other linearly with regard to their in- and output voltage and current. It is common to define one port as a reference port. There are multiple parameters that can be used to describe *N*-port networks. For example, impedance parameters relate input current to output voltage at each port, admittance parameters relate input voltage to output current, and scattering parameters relate forwards-traveling voltage waves to their backwards-traveling counterpart. [17, secs. 2.1, 2.2]
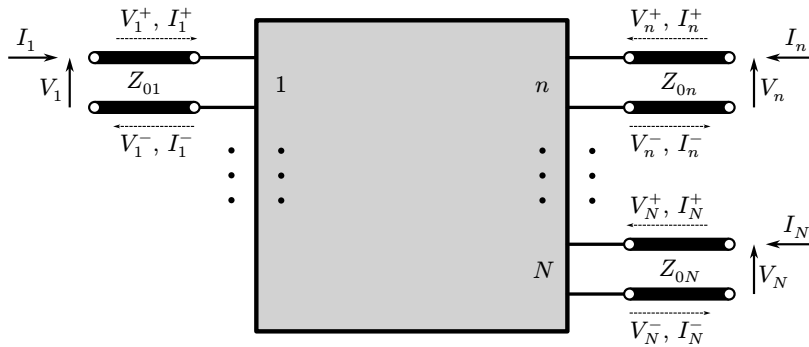
Figure 2.3: Schematic of a *N*-port network. Every port is connected to a transmission line with an incident and reflected wave, for both the voltage and current respectively. Adapted from [17, fig. 2-16].

The scattering parameters are of particular interest as they are a generalization of the wave reflection coefficient introduced in Sec. 2.2.1 and defined similarly. It is possible to define the so-called scattering

parameter matrix $\underline{\mathbf{S}}$ as follows [17, eqs. 2.109–2.111]:

$$
\begin{pmatrix} V_1^- \\ V_2^- \\ \vdots \\ V_N^- \end{pmatrix} = \begin{pmatrix} S_{11} & S_{12} & \cdots & S_{1N} \\ S_{21} & S_{22} & \cdots & S_{2N} \\ \vdots & \vdots & \ddots & \vdots \\ S_{N1} & S_{N2} & \cdots & S_{NN} \end{pmatrix} \begin{pmatrix} V_1^+ \\ V_2^+ \\ \vdots \\ V_N^+ \end{pmatrix} \tag{2.43}
$$

$$
\mathbf{V}^- = \underline{\mathbf{S}} \mathbf{V}^+ \tag{2.44} \qquad\qquad S_{ij} = \left. \frac{V_i^-}{V_j^+} \right|_{V_k^+ = 0 \text{ for } k \neq j} \tag{2.45}
$$

For a one-port network, S_{11} is defined exactly as the wave reflection coefficient for a transmission line derived in Eq. (2.38). Usually, the scattering parameters are normalized to a real transmission line impedance[4] R_0. Let $^{\mathrm{N}}\underline{\mathbf{S}}$ be this normalized scattering parameter matrix. Sometimes it is desirable to calculate the scattering parameters with respect to a different, and not necessarily real impedance. It is possible to renormalize the scattering parameters at each port to the desirable reference impedance Z_{0i} via the generalized scattering parameter matrix $^{\mathrm{G}}\underline{\mathbf{S}}$, which can be calculated as follows, assuming that $R_0 > 0$ [17, eqs. 2.132–2.134]:

$$
^{\mathrm{G}}\underline{\mathbf{S}} = (\underline{\mathbf{D}}^*)^{-1}(^{\mathrm{N}}\underline{\mathbf{S}} - \underline{\mathbf{\Gamma}}^*)(\mathbf{1} - \underline{\mathbf{\Gamma}}\,^{\mathrm{N}}\underline{\mathbf{S}})^{-1}\underline{\mathbf{D}} \tag{2.46} \qquad \Gamma_i = \frac{Z_{0i} - R_0}{Z_{0i} + R_0} \tag{2.48}
$$

$$
D_{ii} = |1 - \Gamma_i^*|^{-1}(1 - \Gamma_i)\sqrt{1 - |\Gamma_i|^2} \tag{2.47} \qquad D_{ij} = 0 \text{ for } i \neq j \tag{2.49}
$$

For a one-port system, the result simplifies significantly to:

$$
^{\mathrm{G}}S_{11} = \frac{^{\mathrm{N}}S_{11} - \Gamma_1^*}{1 - \Gamma_1\,^{\mathrm{N}}S_{11}} \tag{2.50}
$$

Just like the wave reflection coefficient, scattering parameters directly relate to the power transfer between ports. When describing antenna networks, it is also common practice to relate the power transfer between the antennas via scattering parameters. From the definition in Eq. (2.45) one can infer that a scattering parameter of $|S_{ij}| = 1$ indicates that all outgoing power from port (or antenna) j is received at port (or antenna) i without any losses and if $|S_{ij}| = 0$ then no outgoing power from j is received at i. Explicitly, S_{ii} is referred to as the wave reflection coefficient at port i, and S_{ij} (with $i \neq j$) as the wave transmission coefficient from port j to port i [12, p. 45]. Minimizing the scattering parameter's magnitude is therefore a possible approach to optimize the bow-tie antennas geometry for the use case outlined in Sec. 1.

Scattering parameters are preferably given in decibel units, which can be converted as follows [12, p. 46]:

$$
S_{ij}\big|_{\mathrm{dB}} = 20 \log_{10}(S_{ij}) \tag{2.51}
$$

The use of decibel is avoided throughout the thesis and the equation is merely here for the sake of completion.

2.2.3 The Dipole Antenna

Simply speaking, an antenna is a structure between a guided wave and electromagnetic waves in free space. With the theoretical background from the previous sections, it is now possible to describe the working principle of antennas. Generally, there is a distinction between resonant and traveling-wave antennas, but as only the former types are required for the thesis, the working principle of the latter is

---

[4]In engineering $50\,\Omega$ are commonly used as reference impedance, as most commercially available general purpose coaxial cables have a characteristic impedance of either $50\,\Omega$ or $75\,\Omega$.

omitted [19, secs. 4.3, 4.4]. Several other antenna properties are irrelevant as well, because for the scope of this thesis it is only relevant to understand which properties in a good antenna differ from those of a bad antenna for the experimental setup introduced in Sec. 1.

For engineering purposes, they are commonly connected to transmission lines and can be modeled as a one-port network, comparable to Fig. 2.2. It is therefore possible to associate an impedance Z_A (which in turn depends on properties like the geometry and size of the antenna and several other properties) to the antenna at the feed point where the transmission line connects. [20, secs. 2-1–2-3, 2–32, 10–1]

It is necessary to make a distinction between the electromagnetic fields close to the antenna versus at distance. The space around an antenna is therefore divided into sub regions. In close vicinity of the antenna, the reactive near-field dominates. Inside the near-field region (also called Fresnel zone) the electromagnetic fields interact strongly with the antenna, which requires a full spatial description of the fields to describe interacting effects. The near-field region ends at approximately the Fraunhofer distance, which is given as [20, eq. 2-31(1)]:

$$\frac{2D^2}{\lambda} = \frac{2D^2 \nu}{c} \tag{2.52}$$

Hereby, D is the largest dimension of the antenna, λ the operating wavelength in free space, and ν the corresponding frequency of the electromagnetic radiation. At this distance the far-field region (also called Fraunhofer zone) begins. In the far-field region, all emitted radiation is directed radially outwards, with the radiation pattern staying invariant. The radiation pattern is only dependent on the angular direction of emission, with the amplitude of the fields decreasing roughly proportional to $\propto 1/\text{distance}$, and the radiated power decreasing with $\propto 1/\text{distance}^2$. Occasionally, there is a distinction between near-field and Fresnel zone, where the near-field region refers to the strongly interacting fields, and the Fresnel zone to primarily radiating fields which are not necessarily in phase. [20, sec. 2-31][21]

Especially for resonant antennas, the efficiency of an antenna for electromagnetic fields at a certain frequency is heavily dependent on the geometry of the antenna. There are notable special cases for antennas of infinite size, which are frequency independent in their resonance behavior.

One of the simplest types of resonant antennas is the half-wave dipole antenna. It consists of two infinitely thin wires[5] with a combined length of $\lambda/2$, which are fed at their center point. By applying a sinusoidal current with matching frequency to the feed, the moving charges create electromagnetic fields as described by Maxwell's equations[6]. The length of the antenna ensures that the oscillating charges are resonant at the matching frequency. The operation principle can therefore be extended to lengths that are integer multiples of $\lambda/2$. For a dipole antenna of length L the resonant wavelength $\lambda^\star$ can easily be calculated from the following relationship:

$$L = \frac{\lambda^\star}{2} \quad \Leftrightarrow \quad \lambda^\star = 2L \tag{2.53}$$

If, however, the sinusoidal currents are not varying at a matching frequency, the resonance condition is not fulfilled and the antenna performs poorly. The geometry of a dipole antenna ensures that the resulting electric fields are polarized along the movement of the charge carriers (see Fig. 2.4) [20, secs. 2-34–2-37]. [20, secs. 5-1–5-5][21]

---

[5]Or sufficiently thin wires, with measurements suggesting that a dipole is thin if the diameter of the conductor is less than $\lambda/100$. [20, sec. 5-5]

[6]The resulting fields could, for instance, be calculated via Jefimenko's equations from Eq. (2.22) and Eq. (2.23), but are omitted in the following as the solution does not contribute to the fundamental concepts that are required for the thesis.
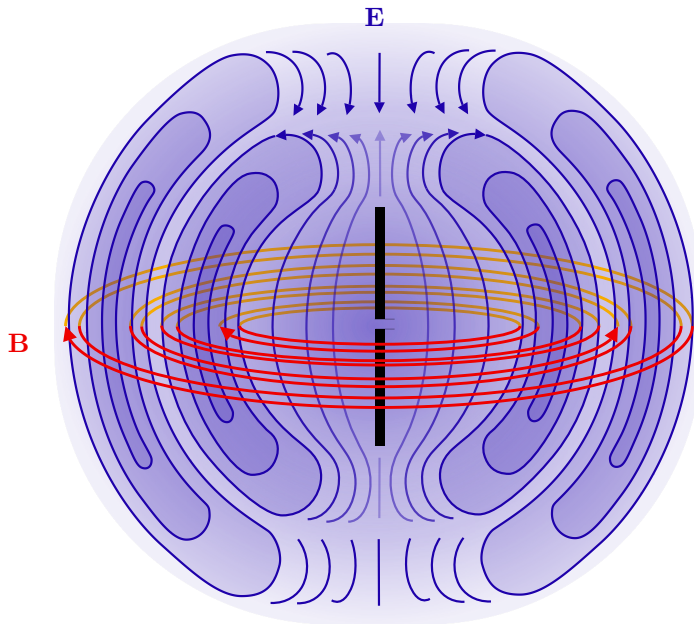
Figure 2.4: Schematic of a transmitting dipole antenna with visualized electric and magnetic fields created by the moving charge carriers inside the conductor. The emitted electric fields are exclusively vertically polarized. From [22].

An important assumption is the principle of reciprocity. It states that the receiving and transmitting of an antenna are identical[7], for example the resonance frequency, bandwidth, impedance, or polarization. The reciprocity theorem is, however, not limited to the previously listed properties. This is a logical conclusion from the fact that if an antenna can transmit or receive electromagnetic waves, it is plausible that the reverse process is also possible. Conveniently, it is therefore possible to study both the transmitting and receiving qualities of an antenna to infer the properties of interest. [20, sec. 10-2]

To summarize, in order to determine the most suitable antenna design, one must ensure that the geometry fulfills the resonance condition of the studied design for the arising currents at the desired frequency or frequency range. Additionally, it is necessary to have the antenna impedance matched at the interface between feed and transmission line (or in the case of the experiment outlined in Sec. 1 impedance matched to the sensing element) to minimize wave reflection and maximize power transfer.

2.2.4   The Bow-tie Antenna

The bow-tie is a geometrical variation of the dipole antenna with several advantages over the simpler design of the dipole. Not only are bow-tie antennas also very simple in design (see Fig. 2.5), but additionally have broad-band impedance. Originally, they have been used for radar and communication applications, but recently they have been utilized in similar terahertz detection experiments with MATBG as outlined in Sec. 1, which makes it the prime candidate for a suitable antenna design for the experimental setup at hand. [1, 9, 23, 24]

Hereby, the current distribution is assumed to be shaped as in Fig. 2.6. Unlike for the dipole antenna, it is not possible to establish an exact relationship between solely the length and resonance wavelength of a bow-tie antenna (or any non-thin wire antenna in general) [21]. However, the following relationship between length L and resonance wavelength $\lambda^\star$, similar to Eq. (2.53), can be established:

$$L < \frac{\lambda^\star}{2} \quad \Leftrightarrow \quad \lambda^\star > 2L \tag{2.54}$$

For an infinitely thin bow-tie antenna of infinite length on a dielectric substrate with $\mu_\mathrm{r} = 1$, the impedance becomes a function of antenna's flare angle and is no longer dependent on the frequency.

---

[7]This is only true for antennas with linear behavior. For instance, an antenna made of non-linear material would not necessarily fulfill the reciprocity theorem. [21]

(a) flat (b) round (c) modified
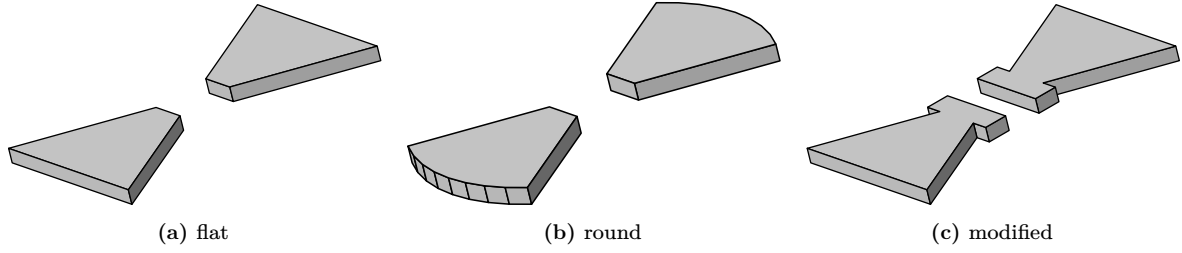
Figure 2.5: Variations of the flat bow-tie antenna design are possible, such as a geometry with round edges as explored in [23] or modified gap as in [25, 26].


(a) type-1 (b) type-2
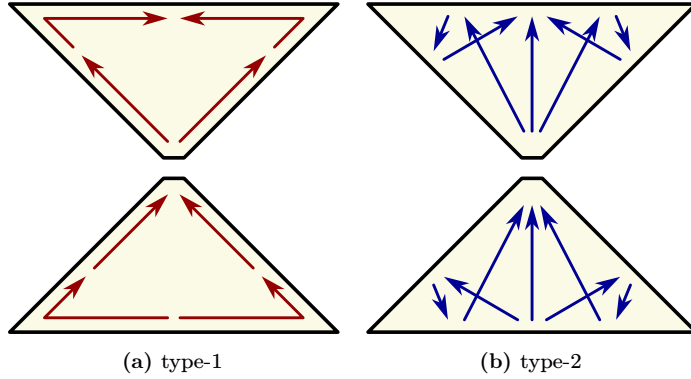
Figure 2.6: Diagram of the primary currents that arise within a flat-edged bow-tie antenna. It is evident that the geometry (unlike a dipole antenna) permits the existence of multiple current distributions. (a) Type-1 currents mostly flow along the edges of the radiator. Adapted from [23, fig. 2a]. (b) Type-2 currents are reflected from the edges multiple times in the antenna. Adapted from [23, fig. 2b].

This behavior is explainable via Rumsey's principle, which states that an infinite length antenna operates independent of the wavelength the antenna is driven at, and merely depends on the angle of the geometry only, because the dimensions of the antenna are invariant under scale, and therefore appear to be identical at every wavelength [20, sec. 15-2]. In reality, this holds true if the length of the antenna is large when compared to the wavelength [23]. Rutledge et al. [27] calculated the impedance of a bow-tie antenna as a function of the flare angle θ (compare to Fig. 3.2 for the flare angle's geometrical definition), plotted in Fig. 2.7, as [27, eq. 10]:

$$Z_{\mathrm{A}} = \sqrt{\frac{2\mu_0}{\varepsilon_0(1+\epsilon_{\mathrm{r}})}} \cdot \frac{K(k)}{K'(k)} \tag{2.55}$$

where $K(k)$ is the elliptical integral of the first kind, $K'(k) = K(\sqrt{1-k^2})$, and $k = \tan^2\left(\frac{\pi-\theta}{4}\right)$.
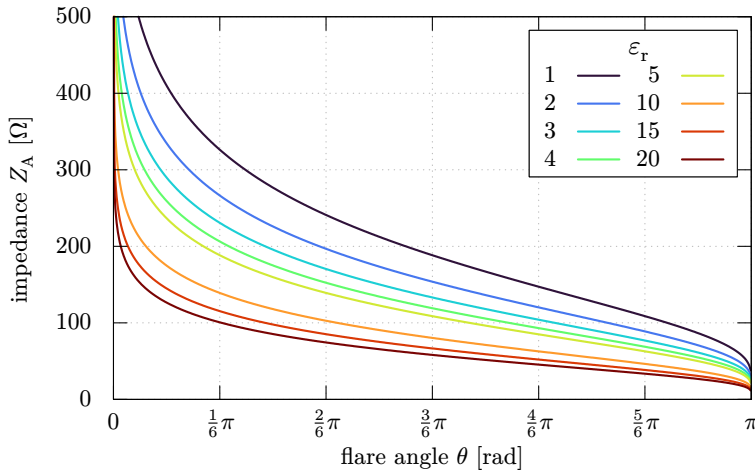
Figure 2.7: Plot of Eq. (2.55) for various values of ε_{r}. The resulting values for $Z = R + iX$ are positive, as the reactance is equals 0 for all values of the flare angle.

Compton et al. [24] derived a more generalized version of this equation for a bow-tie antenna of finite length by analyzing the current modes within the antenna, which requires a decomposition of the

current profile into current eigenmodes. The calculations are vastly more complex and not required for the antenna's design process in this thesis and are therefore omitted.

Even though an analytical solution for the input impedance exists, simulations are required to account for more degrees of freedom in the antenna, such as antenna thickness and gap size. Furthermore, the input impedance alone is not a suitable indicator for the antenna's quality, and there are always deviations between the theoretical results and actual physical properties of a real antenna. Therefore, finite element analysis is, in this case, the preferred method of choice to obtain the most optimal antenna geometry.

3 Simulation

Simulations are a necessity for the task of designing a suitable antenna, as the parameters of interest for the bow-tie antenna have no analytical solution, at least to the extent that would be required here. For extreme cases, such as the infinite length scenario, solutions exist as outlined in Sec. 2.2.4 but are far from being reliable for structures at approximately the size of $\lambda/2$. However, finite element simulations should be able to provide the quantities of interest reliably, presuming that the simulation model is approximating the real-world scenario well enough. For this thesis, the simulation software of choice is *COMSOL Multiphysics* [28] in combination with the *RF Module* addon. Albeit intended for radio frequencies, as the name of the extension suggests, it is possible to extend the simulations towards the Terahertz regime, as it has been successfully used in the modeling process of receiving antennas for similar or other experimental configurations like the one outlined in Sec. 1. [8, 25, 26]

As of *COMSOL* version 6.2.0.339, its benefits include a beginner-friendly GUI, extremely versatile solver capabilities with simulations being possible on virtually any regular desktop computer, and ongoing support for the software via regular updates. On the downside, one needs to purchase a rather expensive license to get basic simulation capabilities and extension modules have to be bought separately to extend the regular user experience. Furthermore, *COMSOL* does not support GPGPU unlike software from competitors, which means that it is rather difficult to significantly improve computation time and resource demand with conventional consumer-grade hardware.

The principle of the finite element method is to divide a to-be-solved problem into small elements, the so-called finite elements, effectively discretizing the problem which in turn allows for the underlying differential equations governing the physics of the model to be solved numerically. For the antenna model, a special case of Maxwell's equations is solved. Because the terahertz source in the experiment is monochromatic and tunable, only the frequency response behavior of the antenna is of interest. When assuming harmonic time dependence of the electromagnetic fields, they can, in complex representation, be written as [12, p. 83, 84]:

$$\mathbf{E}(t,\mathbf{x}) = \mathbf{E}(\mathbf{x})e^{i\omega t} \qquad (3.1) \qquad\qquad \mathbf{B}(t,\mathbf{x}) = \mathbf{B}(\mathbf{x})e^{i\omega t} \qquad (3.2)$$

This simplifies any partial time derivative within Maxwell's equations to a multiplication with $i\omega$, because now only the spatial distribution of the fields is of interest, as the time dependence of the resulting fields is trivial. Similar to Eq. (2.29) and Eq. (2.30), the fields $\mathbf{E}(\mathbf{x})$ and $\mathbf{B}(\mathbf{x})$ are referred to as phasors. *COMSOL* refers to this process as a frequency domain study. This approach, however, is limited to a single frequency at a time and requires the fields to have no additional time dependence besides the assumed harmonic one. If the model is not stable when subjected to a harmonic time dependence (for example, if there are transitions between different states of the model under the given boundary conditions), the simulation cannot converge and is therefore limited to steady-state models only. For cases like this, *COMSOL* provides capabilities to solve a model in the time domain instead of the frequency domain, the latter one being fully sufficient for this intended application. [12, p. 17]
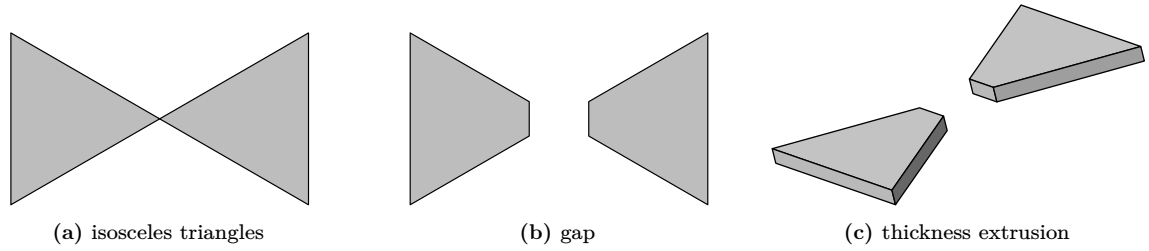
3.1 Geometry

The actual geometry of the antenna is fairly simple, with only a handful of parameters being required to describe the exact configuration. The bow-tie antenna will be evaporated onto dielectric substrate after the design process is finished, and is therefore extremely flat compared to the other spatial dimensions of the antenna. The initial idea for the two-dimensional parametrization of the bow-tie antenna was to start with an isosceles triangle aligned along the x-axis, with the tip placed at the

origin of a three-dimensional coordinate system, and subsequently mirrored directly at the tip to get the characteristic bow-tie shape as in Fig. 3.1a.

Proceeding from that configuration, a rectangular section is cut from the center of the geometry creating a gap like in Fig. 3.1b, which is the feed of the antenna where the graphene sample will be placed later on.

At last, the two-dimensional design is extruded equally in both directions along the z-axis to add thickness to the antenna in Fig. 3.1c, even though the antenna can mostly be considered two-dimensional apart from the implemented simulation model.

The fully parametrized geometry can be seen in Fig. 3.2.

(a) isosceles triangles   (b) gap   (c) thickness extrusion

Figure 3.1: Step-by-step creation of the bow-tie antenna geometry explored in this thesis.
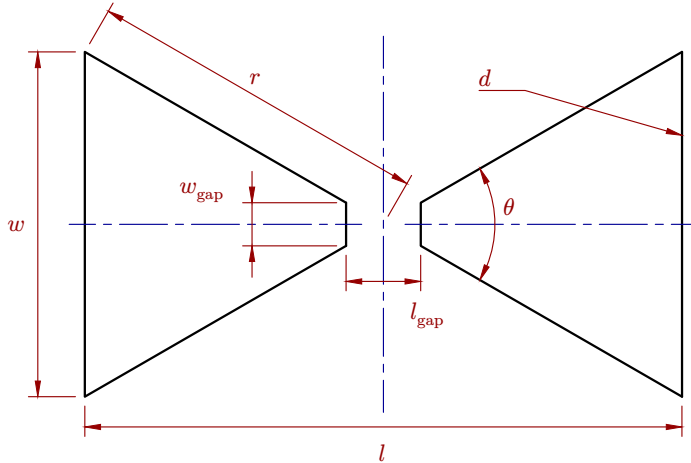
Figure 3.2: Top view of the fully parametrized bow-tie antenna geometry. The blue dashed lines represent two of the three symmetry planes. Albeit not visible directly, d is the thickness of the antenna. The parametrization as shown is overdetermined and introduces the geometrical constraints in Eq. (3.3) and Eq. (3.4). Adapted from [29].

A configuration like this exhibits three conveniently positioned symmetry planes (the xy-, yz-, and zx-plane, all three of them intersecting the coordinate system's origin) visualized in Fig. 3.2, which can be utilized to drastically reduce the simulation domain in size and in turn also the computational power required to solve the model for a given parameter set.

The chosen parametrization merely exhibits four degrees of freedom (two from the isosceles triangle, one from the rectangular section in the center, and one from the extrusion along the z-axis), which does not make the model overly complex and allows to systematically study the effects of each individual degree of freedom. Because the antenna is flat compared to the other dimensions of the geometry, the thickness will remain fixed at a value of $d = 60\,\text{nm}$ throughout the thesis for all simulations while varying all other parameters, as the effect on the antenna thickness should be negligible, considering that $d \approx \lambda/5000$ at 1 THz. The three remaining degrees of freedom are not uniquely defined, therefore the parameters l, l_g, and θ are (for convenience) chosen as the primarily varying parameters describing the antenna's geometry. By geometrical considerations, the remaining parameters have to satisfy the following relations and constraints:

$$\tan\left(\frac{\theta}{2}\right) = \frac{w}{l} = \frac{w_{\mathrm{g}}}{l_{\mathrm{g}}} \qquad (3.3) \qquad\qquad \cos\left(\frac{\theta}{2}\right) = \frac{l}{2r} \qquad (3.4)$$

3.2 Antenna Model

Similar to conventional CAD software, *COMSOL* requires the whole simulation model to be constructed out of primitives, such as circles, rectangles, and polygons in two dimensions and their three-dimensional equivalents of spheres and rectangular parallelepipeds, only to name a few. By carefully combining elements using various operations and transformations, one can create virtually any desirable geometry[8] for up to three spatial dimensions.

The full model does not only consist of the antenna itself, but also includes the free space surrounding it and the boundary conditions at the outer regions of the simulation domain, as seen in Fig. 3.3.
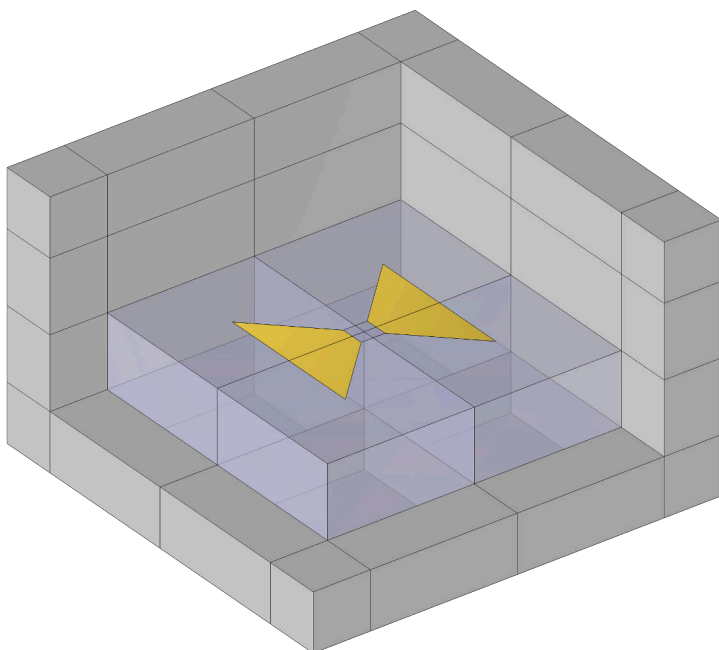
Figure 3.3: The whole simulation domain is shown, with some parts being hidden to improve visibility of the model. The color of the conducting material of the antenna is gold, the vacuum filling the free space transparent blue, and the boundary of the simulation model gray.

Once the geometry of the full model has been built, it is necessary to assign physics and material properties to the resulting domains. It is crucial to choose a suitable configuration that mimics the real to-be-studied physical process as good as possible. The only material constants that are required for the simulations are those introduced by the three constitutive relations given in Eq. (2.5) to Eq. (2.7), namely the relative permittivity ε_{r}, the relative permeability μ_{r}, and the conductivity σ. [12, eq. 3-3, p. 82]

One would logically assign the material constants from the real-world scenario to the model, if possible. However, it turns out that the material properties of interest for the substrate and other materials used in the fabrication process are, at low temperatures, heavily dependent on purity, making it nearly impossible to determine the properties from material databases or data sheets. Effectively, this presents two reasonable options, namely to either infer the necessary constants at room temperature from material databases, or use a simplified model where the antenna is a perfect electrical conductor suspended in vacuum. An additional downside to the former approach is that not all required material constants for the substrate used for fabrication are listed in the manufacturer's data sheet, which would require further speculation regarding the correct values and introduce new inaccuracies on the way.

---

[8]In the classical sense of a Euclidean space. It is noteworthy that *COMSOL* does not directly support non-Euclidean or non-orientable geometries, recently however Lv et al. [30] successfully demonstrated workarounds for some of the constraints in wave optics simulations.

No matter the choice, this would mean trading one inaccuracy for another, so the decision was to choose the latter option, which might even find broader application compared to a model that would be limited to likely wrong material constants and restricted a very specific fabrication process and use case. Besides, there is no choice between different substrates and conducting material during the fabrication process due to the reasons outlined in Sec. 5.

Lastly, the boundary conditions of the system have to be configured. The simulation domain itself is finite in size, so somehow the physics at the outer border of the domain must be accounted for in a realistic manner. For the model presented here, the boundary was configured to perfectly absorb any outgoing radiation, effectively emulating something like an infinitely large simulation space. The corresponding feature in *COMSOL* is the perfectly matched layer (in short PML), which essentially acts as an ideal anechoic chamber without any back reflection of electromagnetic radiation. The thickness of the perfectly matched layer is insignificant, but the distance to the antenna can introduce slight changes in the computed solution and should therefore be ideally placed at half the Fraunhofer distance or higher. [12, p. 147, 148]

To have *COMSOL* treat the conductor as an antenna, it is required to configure a boundary condition inside the gap where the sensing element is to be placed, which acts as the feed of the antenna with a virtually connected transmission line. Hereby, the lumped port feature of *COMSOL*, visualized in Fig. 3.4, has been utilized to achieve this effect. The equivalent electrical circuit of this configuration depends on whether the antenna is simulated to be receiving or transmitting, but generally it is possible to probe various physical and electrical quantities and properties related to the configuration of the system. Independent of a transmitting or receiving antenna configuration, it is necessary to set the characteristic impedance of the virtual transmission line, which is set to $50\,\Omega$ by default.



(a) antenna   (b) antenna feed
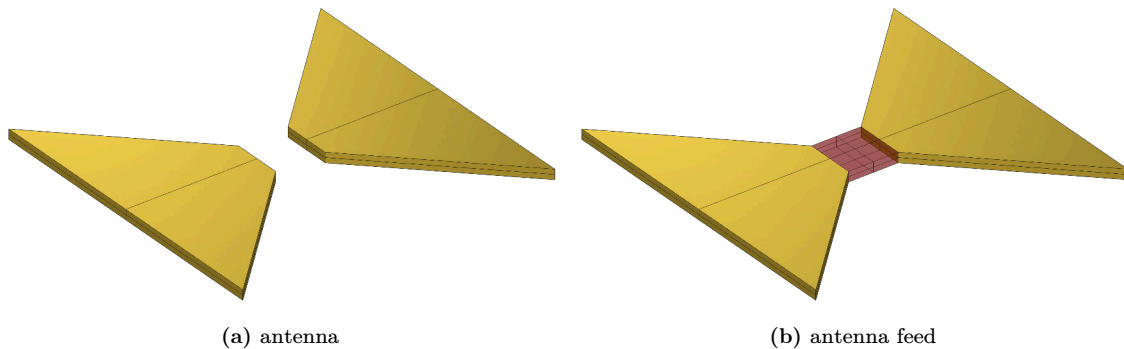
Figure 3.4: To improve visibility the thickness of the antenna is exaggerated and not to scale. (a) Antenna without the surrounding simulation model. (b) Virtual feed of the antenna, colored red to improve visibility, which is placed inside the gap of the antenna, with the surface of the lumped port extending and connecting the two lobes.

It is important to note that the lumped port is merely the simplification of a real antenna feed and is only an accurate approximation if the phase variations of electromagnetic waves inside the gap and electric signals in the virtual transmission line at the boundaries of the port are negligible, which is the case if the gap is small compared to the operating wavelength. [12, p. 225, 226]

To match the frequency range of the terahertz source used in the experiment, the model has been studied for frequencies between $0\,\text{THz}$ to $2\,\text{THz}$. This concludes the fundamental configuration of the model. Depending on the exact demands for the simulation, there mostly need only minor changes to be made to the configuration of the system.

3.2.1 Transmitting Scenario

Motivated by the reciprocity theorem, a first simulation model was set up to study the transmitting properties of the bow-tie antenna. In this configuration, the virtual antenna feed supplies the antenna with alternating current, with an equivalent electrical circuit as in Fig. 3.5 [31, sec. 10.3]. Via the simulation of a transmitting antenna, it is possible to infer the antenna's wave reflection coefficient at the frequencies of interest. Via Eq. (2.50), it is possible to change the default reference impedance of $50\,\Omega$ to any other desirable (and not necessarily real) impedance. This drastically reduces the demands on the model, as it is sufficient to simulate the model with varying frequency at a fixed impedance.
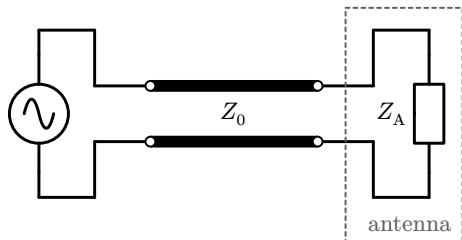
Figure 3.5: Equivalent circuit for the transmitting scenario. The amplitude of the alternating voltage was set to $1\,\text{V}$ for convenience, as the calculated scattering parameters are independent of this value due to linearity of the simulation model.

The model was configured to solve for the full electromagnetic fields generated by the antenna inside the simulation domain. In *COMSOL*, this is referred to as the full field formulation. [12, p. 205]

It is possible to optimize the model via symmetry considerations, such that only 1/8 of the simulation domain needs to be simulated. By considering that the bow-tie antenna is a geometrical variation of the dipole antenna and assuming that the resulting fields are somewhat similar to those as in Fig. 2.4, one can define symmetry conditions inside *COMSOL* to reduce the model size. As already established before in Sec. 3.1, the geometry of the bow-tie antenna itself has three symmetry planes. *COMSOL* provides additional boundary conditions for two symmetry types, where the electric and magnetic fields at a plane have only a normal component to the surface with no tangential component, visualized in Fig. 3.6. [12, p. 172, 173]
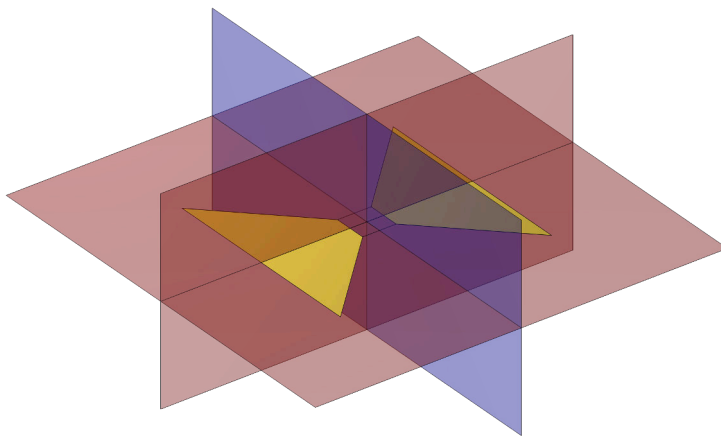
Figure 3.6: Visualization of the symmetry planes. The two red planes represent the perfect magnetic conductor symmetry condition, which require the tangential component of the magnetic field to be zero. Likewise, the blue plane represents the perfect electric conductor symmetry condition and requires the tangential component of the electric field to be zero.

By comparison of two simulations with identical antenna geometry, it has been concluded that the computed results for S_{11} via this reduced model are (within the specified relative error margins) equal to those computed via the full model.

3.2.2 Receiving Scenario

For a more in-depth analysis of the model, it is good practice to validate the simulations of the transmitting configuration by comparing the results with those of a receiving configuration, at the cost of higher computational effort. The receiving model was set up to use the scattered field formulation,

which computes the total electric field $\mathbf{E}$ that is decomposed into two components as follows [12, p. 34, 35]:

$$\mathbf{E} = \mathbf{E}_{\mathrm{b}} + \mathbf{E}_{\mathrm{r}} \tag{3.5}$$

Hereby, $\mathbf{E}_{\mathrm{b}}$ is a user-defined phasor for the electric field, and $\mathbf{E}_{\mathrm{r}}$ the relative field such that the sum of both fulfill Maxwell's equations. For the sake of simplicity, the background field was specified to be a plane wave traveling in $-z$ direction, which should be a good approximation to the real experimental setup, considering that the whole simulation domain is only the size of roughly one full wavelength λ_0. Via Eq. (2.16), the background field equates explicitly to:

$$\mathbf{E}_{\mathrm{b}}(\mathbf{x}) = \mathbf{E_0} e^{i|\mathbf{k}|z} \tag{3.6}$$

$$E_{\mathrm{b}z} = E_{0z} = 0 \tag{3.7}$$

The Jones vector $\mathbf{E_0}$ was configured to be linearly polarized along the x-axis (which is now referred to as 0° polarization) with a complex field amplitude of $|\mathbf{E_0}| = E_0 = 1\,\mathrm{V\,m^{-1}}$. The z component of $\mathbf{E_0}$ is trivially zero, reducing the Jones vector to a two-element vector for the E_{0x} and E_{0y} component respectively:

$$\mathbf{E_0} = \begin{pmatrix} E_{0x} \\ E_{0y} \end{pmatrix} = E_0 \begin{pmatrix} 1 \\ 0 \end{pmatrix} \tag{3.8}$$

The choice of the field amplitude is insignificant, because the electric field's solution to Maxwell's equations scales linearly with the field amplitude, since the model does not regard any nonlinear effects or material properties the way it has been configured. This behavior has been tested and confirmed via simulations. Therefore, the value of $1\,\mathrm{V\,m^{-1}}$ has been chosen for convenience to allow for easier normalization of the results, if required.

The introduction of a background field via the scattered field formulation prevents the definition of scattering parameters because the model can no longer be abstracted to a N-port network, but conveniently allows to directly infer the power delivered to the antenna feed P_0 with an equivalent circuit as depicted in Fig. 3.7 [31, sec. 10.3]. This approach has been successfully utilized to model antennas for similar experiments and is also a more direct and better approach to determine an antenna's suitability. [8]
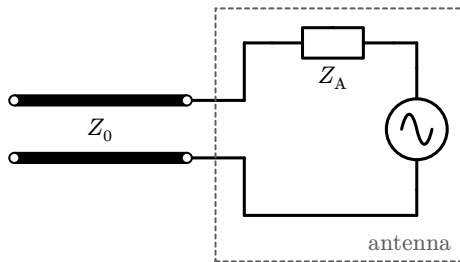
Figure 3.7: Equivalent circuit for the receiving scenario. In this configuration, the antenna acts as a Thévenin equivalent voltage source. As a consequence of the maximum power transfer theorem, the transmission line and antenna have to be impedance matched for maximum performance.

Unlike for the transmitting model, no additional simplifications have been made to reduce computation time via symmetry considerations as to not interfere with the polarization direction of the incident wave. Albeit untested, it should have been possible to define the xy-plane as a perfect magnetic conductor symmetry condition, which would not interfere with the polarization of the incident plane wave in any detrimental fashion.

A significant downside to the receiving configuration was the necessity to simulate the model for different values of the feed impedance due to the lack of a suitable equation (similar to Eq. (2.50) utilized for the transmitting scenario), which would allow to calculate the delivered power from one known reference impedance alone.

3.3 Meshing

After having configured the physics of the model, it is necessary to discretize the problem for it to be numerically solvable in the first place. Meshing refers to the process of subdividing the geometry into smaller elements, in three dimensions specifically tetrahedra, hexahedra, triangular prisms, and pyramids, as shown in Fig. 3.8. In two dimensions, a mesh consists only of triangular and quadrilateral elements. Their size, count, and shape, in combination with their physical coupling, ultimately define the exact set of equations that is solved numerically.

(a) tetrahedron   **(b) hexahedron**   **(c) triangular prism**   **(d) pyramid**
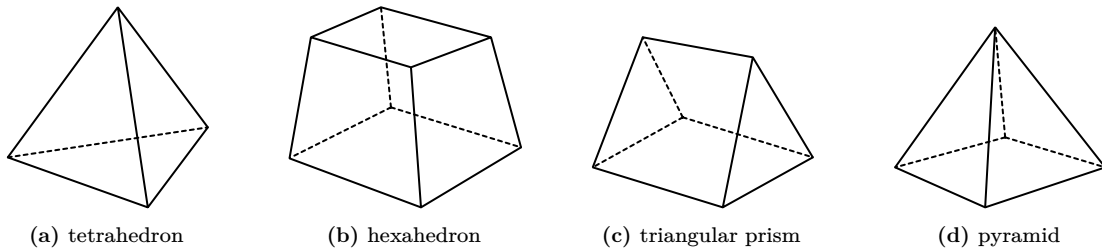
Figure 3.8: The four primitive mesh elements. The amount of vertices, edges, and faces determine the number of degrees of freedom of each element.

For finite element simulations in general, the correct choice of the element size is crucial. A mesh that is chosen too coarse might impact the accuracy of the solution at regions of interest or the entire simulation domain and might even prevent the solver from converging entirely, whereas a finer mesh results in a more accurate solution with increased spatial resolution whilst increasing computational effort and required memory. Balancing these effects is a necessity, especially for lower-end computer hardware. In case of the *RF Module*, the element size should be limited to a fraction of the wavelength and ideally not exceed a size of $\lambda/10$. [12, p. 94–96]

COMSOL provides a default meshing sequence which subdivides the geometry according to built-in rules. For the model at hand, the default routine is not suitable, resulting in elements of bad quality[9], vastly increased computation effort, and occasionally decreased resolution at regions of interest when employed nonetheless. This mostly happens at the antenna itself and nearby regions due to the small thickness along the z-axis compared to the antenna within the xy-plane.

By configuring a custom meshing sequence, it is possible to generate a highly optimized mesh that is in many ways superior to the default sequence. The undesired effects can be mitigated by using a swept mesh for the antenna geometry, the effect being visualized in Fig. 3.9.

(a) unstructured   **(b) structured**   **(c) unstructured**   **(d) structured**   **(e) hybrid**
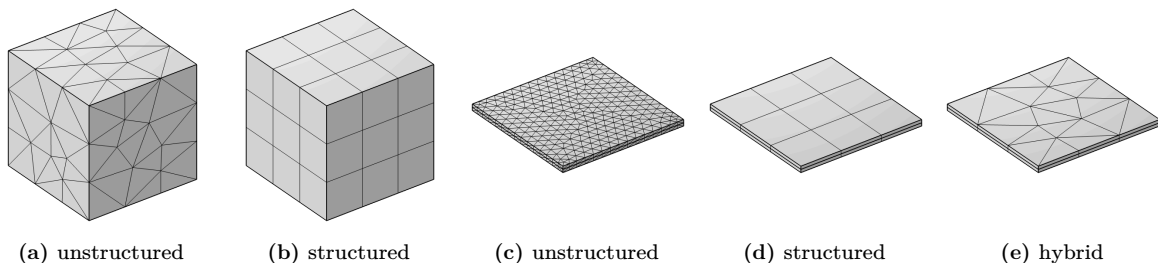
Figure 3.9: Cubes and flat multilayers of equal size meshed via different methods. The cube meshed with an unstructured mesh (a) results in a slightly larger element count compared to a structured mesh (b). In the extreme case of flat multilayers with an unstructured mesh (c) this results in a significantly higher element count. This decrease in element size can be mitigated by using a swept mesh, allowing for a structured mesh (d) or hybrid variant thereof (e) without a significant increase in element count.

---

[9]There are different measures of quality for elements such as skewness or the ratio of volume versus circumference. Independent of the employed measure elements of bad quality can compromise the accuracy of the computed solution. [32, p. 758, 759]

The remaining unmeshed domains can be meshed via techniques similar to the built-in sequence that do not need to be enhanced as much as the sequence for the antenna itself. The final choice for the element size at different parts of the model geometry can be inferred from Tab. 3.1, which are all defined relative to the free-space wavelength λ_0 at the chosen central frequency $\nu_0 = 1\,\text{THz}$, with $\lambda_0 = c/\nu_0 \approx 300\,\mu\text{m}$.

Geometry	Reduced		Full		Method
	min	max	min	max	
Global	$\lambda_0/1000$	$\lambda_0/10$	$\lambda_0/1000$	$\lambda_0/25$	
Port	global	$\lambda_0/200$	global	$\lambda_0/500$	structured + swept
Antenna	global	$\lambda_0/200$	global	$\lambda_0/125$	unstructured + swept
Vacuum	global	global	global	global	unstructured
PML	global	global	global	global	structured + swept

Table 3.1: Mesh size configuration for the model reduced via symmetry planes and the full model respectively, unless specified explicitly otherwise. The structured meshes consist of quadrilateral and hexahedral elements, whereas the unstructured meshes consist of triangular and tetrahedral elements.

3.4 Solver Configuration

At last, the iterative solver requires configuration before the simulation can be started. *COMSOL* provides default presets for the solver, which already work well for the model at hand. Some minor adjustments can be made to further reduce computation time. As already established before, the solver computes the steady-state solution for Maxwell's equations in the frequency domain. For the simulation models computed in this thesis, the fastest solver preset has been chosen and modified.

The bulk simulations of the reduced transmitting antenna model were configured to use the asymptotic waveform evaluation solver, which provides a significant reduction in simulation time without sacrificing accuracy over the whole frequency interval of interest. The asymptotic waveform evaluation solver computes the solution at set frequencies and utilizes Taylor or Padé series expansion to transfer the solution within the specified relative error margins to neighboring frequencies where the solution is not changing significantly (which is often the case for frequencies distant of resonant frequencies). The advantage over the conventional solver is the vast increase in frequency resolution whilst keeping the simulation time nearly constant. For the solver to be applicable, it is necessary to supply a control expression that quantifies the change of the solution over different frequencies. By default, *COMSOL* uses $|S_{11}|$ as control expression. [12, p. 67–69]

The relative error margins have been set to a value of 0.1 compared to the default value of 0.01 to further decrease computation time. By comparing two simulations with different margins, it was concluded that the changes in the computed solution are insignificantly small for the quantities of interest. In combination with the symmetry optimizations made in Sec. 3.2.1, the model takes little time to solve compared to the full receiving antenna model, making it ideal for bulk simulations with many different parameter combinations.

For simulations of the full receiving antenna model, the default solver preset was used with default relative error margins of 0.01, as the asymptotic waveform evaluation solver cannot be applied to the model due to the lack of a suitable control expression, simply because no scattering parameters can be inferred from the receiving antenna model as it has been configured. A small reduction in simulation time is possible when performing simulations with varying parameters, for example frequency or feed impedance, or polarization of the incident plane wave, that do not change the geometry of the model. For such cases, it is possible to reuse the solution of a previously computed step as the initial values for the next iteration process, which saves time, if the solutions at each step do not differ significantly.

4   Results and Discussions

The simulations of the models introduced in Sec. 3.2 have been conducted for various parameter combinations, with the results being presented and analyzed throughout this section.

4.1   Transmitting Scenario

The low simulation time of reduced transmitting model makes it highly suitable for bulk simulations. The model has been studied for all possible parameter combinations listed in Tab. 4.1.

parameter		start	end	step	count
l	[µm]	10	250	10	25
l_{gap}	[µm]	10	60	10	6
θ		$1\pi/6$	$4\pi/6$	$1\pi/6$	4
ν	[THz]	0.1	0.02	2	

Table 4.1: Studied parameter combinations for the transmitting scenario. From the total 600 combinations only 516 are valid due to the geometrically necessary constraint of $l_{\mathrm{gap}} \leq l$ that has to be fulfilled, resulting in 84 invalid combinations that are omitted.

Initially, this vast amount of data proved to be difficult to analyze in an effective manner. Most notably however, the general observation was that larger flare angles are associated with lower antenna impedances, which aligns with the theoretical calculations for a bow-tie antenna of infinite length as demonstrated in Fig. 2.7, and longer antenna lengths with lower resonance frequencies as confirmed with Eq. (2.54). Ultimately, however, only little reliable information could be inferred from the resulting data. For one, it was possible to infer the resonance frequency $\nu^\star$ from the calculated scattering parameters and the impedance of the antenna Z_{A} at each studied frequency. The data for the S_{11} parameter was obtained at a constant feed impedance of $Z_0 = 50\,\Omega$, and via Eq. (2.50) extended to a range of $10\,\Omega$ to $10\,000\,\Omega$.

This data was visualized via three-dimensional plots of S_{11} versus ν and Z_0, such as the one shown in Fig. 4.1. From these plots, it is possible to infer the resonance frequency $\nu^\star$ and corresponding antenna impedance Z_{A} which minimize the value of $|S_{11}|$.

Multiple resonance peaks have been observed, suggesting the existence of resonance frequencies with a high value of Z_{A}, which would be ideal for minimizing the impedance mismatch between the antenna and graphene. To validate these results, preliminary simulations of the receiving model configuration have been made to study the delivered power for varying frequency and feed impedance. From the resulting data, it was concluded that only the first observed resonance peak of the scattering parameter coincides roughly with the resonance peak inferred from the delivered power, whereas the other observed resonance peaks of the scattering parameter at higher frequencies did not produce significant corresponding peaks for the delivered power.

The additional resonance peaks did not behave as expected in regard to the power transmission. Therefore, this apparently flawed approach to simulate transmitting antennas was abandoned in favor of simulating receiving antennas. The only reliable information that can be inferred from the bulk simulations of the transmitting antenna model is a rough estimate of the resonance positions as in Fig. 4.2 for the studied parameter combinations.

4.2   Receiving Scenario

To improve on this previous and seemingly flawed approach, specific parameter combinations for the bow-tie antenna of the receiving model have been studied. From the bulk data obtained in Sec. 4.1
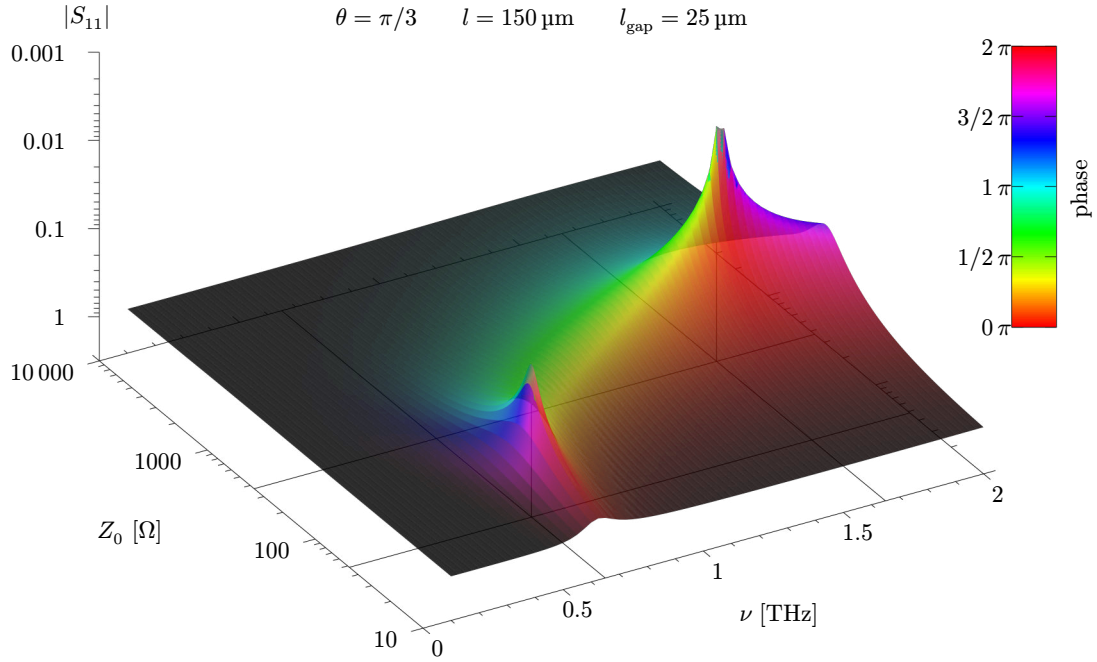
Figure 4.1: Surface plot of S_{11} versus frequency ν and feed impedance Z_0 with reversed z-axis. As scattering parameters are complex-valued, the magnitude of the parameter is encoded into the z-position, and the phase into the color of the plot. Multiple resonance peaks are visible, the first one at roughly $\nu_1^\star \approx 0.65\,\text{THz}$ with $Z_{A,1} \approx 48.0\,\Omega$, and the second peak at roughly $\nu_2^\star \approx 1.65\,\text{THz}$ with $Z_{A,2} \approx 367.5\,\Omega$. At resonance, voltage and current are in-phase, resulting in a real-valued antenna impedance Z_A.
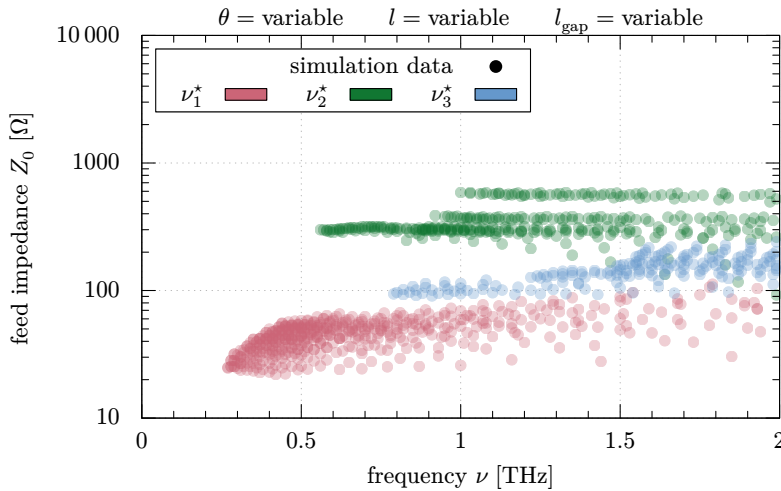
Figure 4.2: Scatter plot of the three lowest resonance frequencies $\nu_i^\star$ with corresponding antenna impedance $Z_{A,i}$, inferred from S_{11} of each parameter combination listed in Tab. 4.1. The resonance frequencies for some simulations are not inside the studied frequency interval of 0.1 THz to 2 THz. The longer the antenna, the more apparent resonance frequencies are found within this interval.

and Fig. 4.2, a parameter combination close to the desired resonance frequency of $\nu^\star = 0.5\,\text{THz}$ has been chosen. The gap length was set to a fixed value of $25\,\mu\text{m}$ due to size limitations in the fabrication process of the sensing element's aspired Hall bar structure. To study the effect of each degree of freedom individually, only one parameter has been varied at once whilst keeping the other parameters fixed. The studied parameter combinations can be inferred from Tab. 4.2.

parameter		fixed	start	end	step
l	[µm]	150	75	300	25
l_{gap}	[µm]	25	10	60	5
θ		$\pi/2$	$1\pi/6$	$4\pi/6$	$1\pi/6$
ν	[THz]		0.1	2	0.025

Table 4.2: Studied parameter combinations for the receiving scenario. The feed impedance Z_0 has been kept constant at a value of $50\,\Omega$ for all but one simulation.

As already mentioned before, the power delivered to the antenna feed P_0 should be a better indicator for an antenna's suitability, as it is a more direct approach to access the quantity of interest compared to the indirect approach via scattering parameters in combination with Eq. (2.42) and the resulting discrepancies with the expectations [8]. The goal for the receiving antenna model was to find trends in the data, which allow to inter- and extrapolate the data to obtain a set of parameters that maximize the delivered power at the desired resonance frequency. When comparing the available degrees of freedom with one another and applying the theoretical fundamentals of the dipole and bow-tie antenna from Sec. 2.2.3 and Sec. 2.2.4, it would be expected that a change in the antenna length and flare angle significantly shift and change the resonance frequency and delivered power due to the increase in surface area and the resulting increase in electrical length, whereas the gap length should leave the resonance frequency roughly invariant, but decrease the delivered power when increasing the distance between the antenna lobes.

For a plane wave with constant amplitude and polarization with a set direction incident on any antenna with linear behavior, it is possible to define the antenna's effective area A_{eff} along the direction of propagation, which conveniently relates the delivered power at the antenna's feed to the intensity of the incident wave as follows [31, eq. 10.3.22]:

$$P_0 = I A_{\text{eff}} \qquad (4.1) \qquad\qquad \langle P_0 \rangle_T = \langle I \rangle_T A_{\text{eff}} \qquad (4.2)$$

The larger the effective area the better is the antenna's ability to receive power from the incident plane wave. By Eq. (4.1) or Eq. (4.2) it is equivalent to maximize P_0 or A_{eff}. The electric field amplitude of the incident wave was kept constant at $|\mathbf{E_0}| = 1\,\text{V m}^{-1}$ for all simulations, yielding $I = 2.654 \times 10^{-3}\,\text{pW/µm}^2$ and $\langle I \rangle_T = 1.327 \times 10^{-3}\,\text{pW/µm}^2$ in combination with Eq. (A.17), Eq. (A.22), and Eq. (A.24). It is evident that the simulation model is therefore entirely independent of the actual chosen electric field amplitude when performing this normalization of the power to generalize the results for an arbitrary intensity of the incident radiation.

Varying Feed Impedance Z_0

To get a general ideal of the effective area's frequency and impedance dependency, the first simulation has been conducted for fixed geometrical parameters with roughly logarithmic-spaced varying values of Z_0 between $10\,\Omega$ to $10\,000\,\Omega$. The resulting data is plotted in Fig. 4.3.

The antenna impedance Z_A is no directly accessible quantity within *COMSOL* for a receiving antenna configuration via the scattered field formulation. To obtain a value for Z_A it is possible to
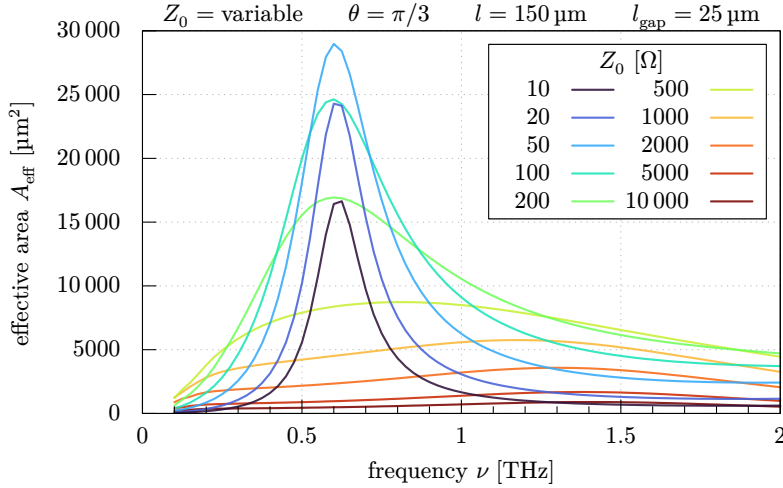
Figure 4.3: Plot of effective area A_{eff} versus frequency ν for varying feed impedance Z_0. The effective area is maximal for a value of Z_0 between $20\,\Omega$ to $100\,\Omega$ at the apparent resonance frequency of $\nu^\star \approx 0.6\,\text{THz}$. For increasing values of Z_0, the maximum value of A_{eff} decreases significantly and shifts towards higher frequencies.

either infer the value from a transmitting configuration like in Fig. 4.1, or alternatively, employ the maximum power theorem for a Thévenin equivalent generator. In the case of the circuit configuration of the receiving antenna like in Fig. 3.7, the maximum power theorem states that the transferred power is maximal, if and only if $Z_0 = Z_A^*$. The equation describing the delivered power can be utilized as a fit function to infer Z_A from the simulation data in Fig. 4.4 in combination with Eq. (4.2), with V_A being the voltage of the antenna acting as a source [16, eq. 2.168]:

$$\langle P_0 \rangle_T = \frac{1}{2} \left| \frac{V_A}{Z_A + Z_0} \right|^2 R_0 = \frac{1}{2} \frac{|V_A|^2 R_0}{(R_A + R_0)^2 + (X_A + X_0)^2} \tag{4.3}$$
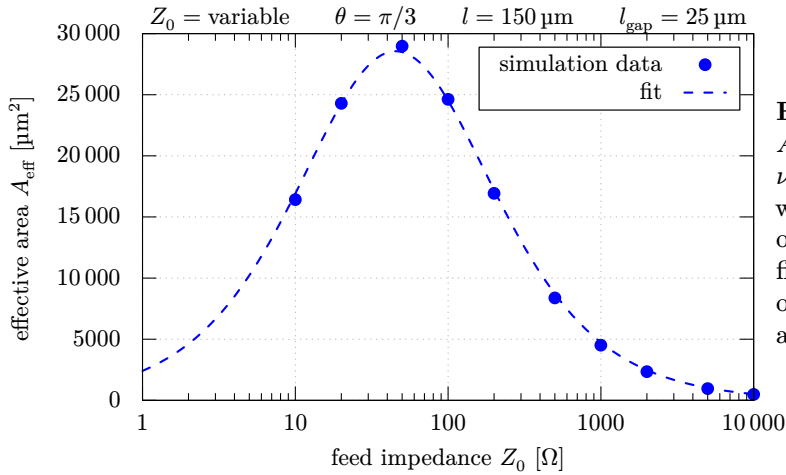
Figure 4.4: Plot of effective area A_{eff} versus feed impedance Z_0 at $\nu = 0.6\,\text{THz}$, fitted via Eq. (4.4), where $|V_A|$ and R_A are constants obtained through fitting. From the fit (with an R^2 value of 0.9992), one obtains $|V_A| = (117.2 \pm 0.9)\,\mu\text{V}$ and $Z_A = (45.3 \pm 0.7)\,\Omega$.

$$A_{\text{eff}}(Z_0) = \frac{1}{2} \frac{1}{\langle I \rangle_T} \frac{|V_A|^2 R_0}{(R_A + R_0)^2 + (X_A + X_0)^2} \Bigg|_{X_A = 0\,\Omega} \tag{4.4}$$

The values for Z_A obtained from the transmitting and receiving configuration are, albeit not equal within the standard error, consistently close enough to one another. A possible explanation is the comparably coarse frequency resolution of $\Delta\nu = 0.025\,\text{THz}$, which results in insufficiently resolved data near the resonance peaks of Fig. 4.1 and Fig. 4.4. Moreover, the reciprocity principle is not entirely fulfilled, considering that a transmitting antenna configuration results in an omni-directional radiation pattern compared to the unidirectional propagation of the incident plane wave of the receiving configuration. Nonetheless, this small deviation adds no significant contribution to the design guidelines

of the bow-tie antenna in this thesis. The same holds true for the different resonance frequencies inferred from the models, both should however be able to provide a sufficiently accurate estimate on the actual resonance frequency of the antenna.

The contact impedance between antenna and sensing element of the detector should thus be minimized as well as possible to maximize the power delivered to the device.
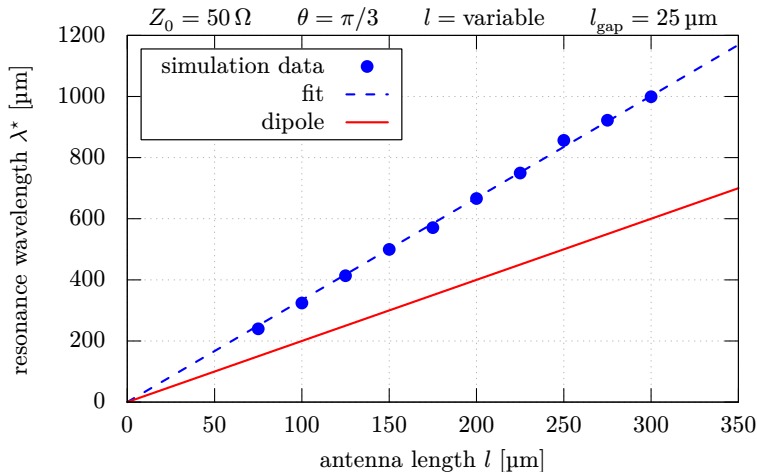
Varying Antenna Length l

The first varied geometrical parameter is the antenna length l, while keeping the feed impedance at a fixed value of $Z_0 = 50\,\Omega$. The resulting data for the antenna's effective area is visualized in Fig. 4.5.
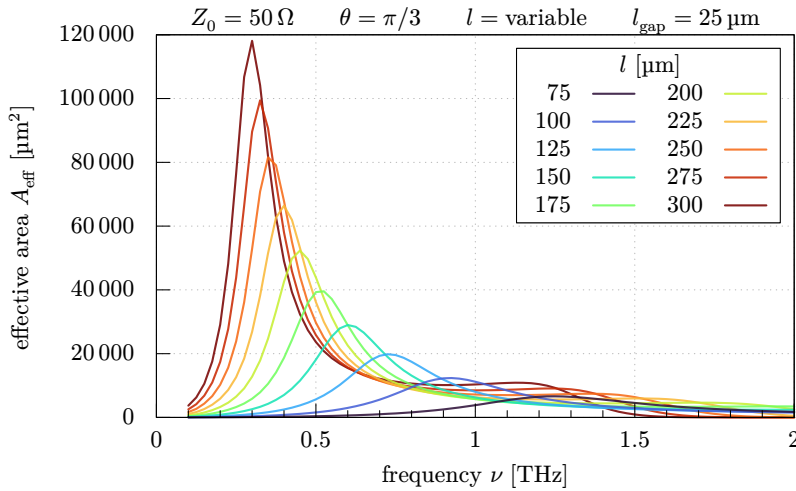
Figure 4.5: Plot of effective area A_{eff} versus frequency ν for varying antenna length l. As expected, the effective area increases together with the actual area of the antenna, with the resonance frequency shifting towards lower frequencies for increased antenna lengths.

Most notably, the shift resonance frequency $\nu^\star$ is best observed by looking at the resonance wavelength $\lambda^\star$ instead. Similarly to the relationship between resonance wavelength and length of a dipole antenna as in Eq. (2.53), the data from Fig. 4.6 also suggests a similar linear relationship between resonance wavelength and length for a bow-tie antenna.

Figure 4.6: Plot of resonance wavelength $\lambda^\star$ versus antenna length l, fitted via a linear function passing the origin of the graph. From the fit (with an R^2 value of 0.998), one obtains a slope of 3.340 ± 0.015.

The proportionality factor inferred from the fit establishes a robust relationship between these quantities, which allows one to infer the corresponding antenna length for any desired resonance wavelength at the fixed parameters for l_{gap} and θ as given in Tab. 4.2.

One other useful observation is the relationship between effective area at resonance and length of the antenna. When l is increased, the actual cross-sectional surface area of the antenna is increased as well, which in turn also increases the effective area of the antenna. Through empirical observations

and trying one finds that A_eff/A is approximately constant for the explored parameter range, where A is the cross-sectional area of the antenna when viewed along the z-direction. For small values of l_gap, a good approximation for A can be obtained geometrically from Fig. 3.1a by approximating the bow-tie antenna as two isosceles triangles without a gap[10] in combination with the constraint in Eq. (3.3):

$$A = \frac{1}{2}lw = \frac{1}{2}l^2 \tan\left(\frac{\theta}{2}\right) \tag{4.5}$$

This expression can be utilized to obtain a suitable fit function which reasonably approximates the relationship between A_eff and l within the simulated parameter range, visualized in Fig. 4.7.
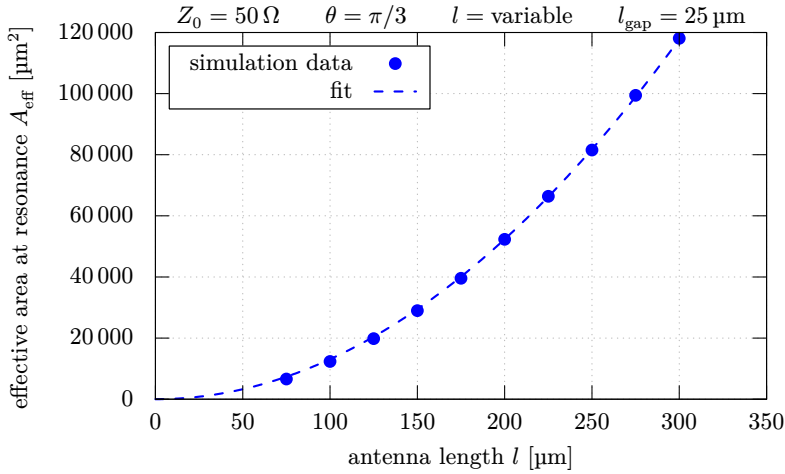
Figure 4.7: Plot of effective area A_eff versus antenna length l at $\nu^\star$, fitted via the empirically obtained expression in Eq. (4.6), where C_1 is a constant obtained through fitting. From the fit (with an R^2 value of 0.9998), one obtains $C_1 = 2.267 \pm 0.006$.

$$A_\mathrm{eff}(l) = \left.\frac{1}{2}C_1 l^2 \tan\left(\frac{\theta}{2}\right)\right|_{\theta=\frac{\pi}{3}} \tag{4.6}$$

The chosen fit function fulfills the physically necessary limit of $\lim_{A\to 0} A_\mathrm{eff} = 0$. Conclusively, the value of l should be maximized as much as possible, as long as the resonance is still matched at the desired resonance wavelength.

Varying Gap Length l_gap

The gap length l_gap was the next studied parameter, with the data visualized in Fig. 4.8.

To describe the relationship between A_eff and l_gap, Wang et al. [26] utilized an empirical fit function to relate the gap length to the electric near-field enhancement for the modified bow-tie antenna design in Fig. 2.5c. The fit function was adapted by multiplying the expression by the area of the gap A_gap, with the latter in combination with Eq. (3.3) evaluating to:

$$A_\mathrm{gap} = l_\mathrm{gap} w_\mathrm{gap} = l_\mathrm{gap}^2 \tan\left(\frac{\theta}{2}\right) \tag{4.7}$$

The utilized fit function fulfills the physically necessary limit of $\lim_{l_\mathrm{gap}\to\infty} A_\mathrm{eff} = 0$. Conclusively, the value of l_gap should be minimized as much as the sensing element's size allows.

Varying Flare Angle θ

At last, the flare angle θ was studied for four selected values, with the results plotted in Fig. 4.10.

---

[10]The exact equation for the cross-sectional area of the antenna as in Fig. 3.1b evaluates to $A = \frac{1}{2}(lw - l_\mathrm{gap}w_\mathrm{gap}) = \frac{1}{2}(l^2 - l_\mathrm{gap}^2)\tan\left(\frac{\theta}{2}\right)$. Therefore the approximation in Eq. (4.5) requires that $l^2 \gg l_\mathrm{gap}^2$.
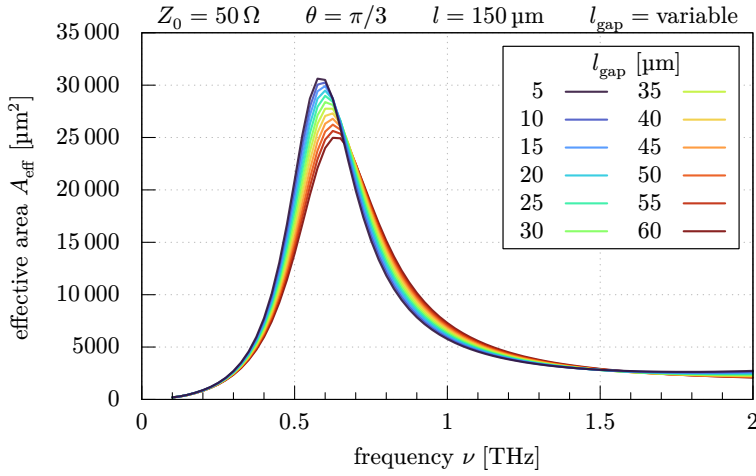
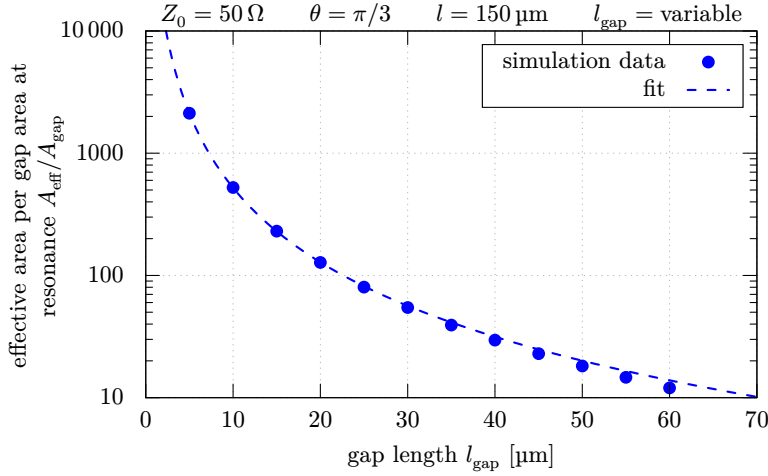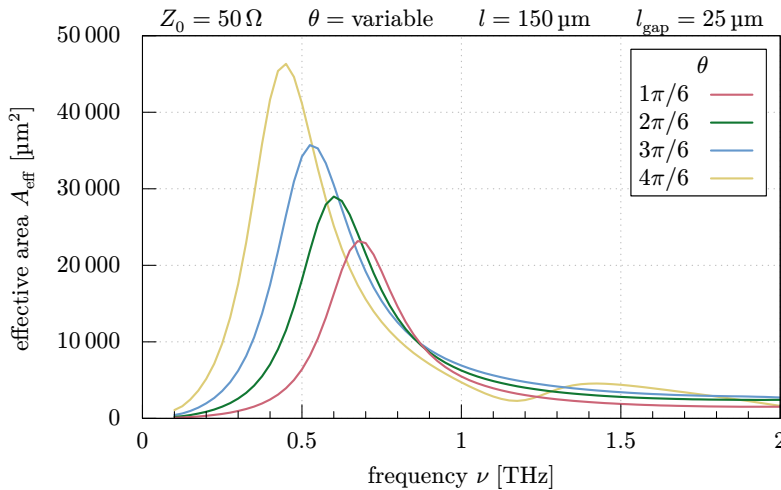**Figure 4.8:** Plot of effective area A_{eff} versus frequency ν for varying gap length l_{gap}. Within the studied parameter regime, the resonance frequency did not change significantly over the studied parameter range, the effective area is however slightly larger for smaller values of l_{gap}.

Figure 4.9: Plot of effective area per gap area $A_{\text{eff}}/A_{\text{gap}}$ versus gap length l_{gap} at $\nu^{\star}$, fitted via the modified empirical expression in Eq. (4.8) from [26, eq. 1], where C_1 and C_2 are constants obtained through fitting. From the fit (with an R^2 value of $0.999\,991$), one obtains $C_1 = (4.55 \pm 0.04)\,\text{mm}^{-1}$ and $C_2 = 2.024 \pm 0.004$.

$$\left.\frac{A_{\text{eff}}}{A_{\text{gap}}}(l_{\text{gap}})\right|_{\theta=\frac{\pi}{3}} = \left(C_1 l_{\text{gap}}\right)^{-C_2} \tag{4.8}$$

Figure 4.10: Plot of effective area A_{eff} versus frequency ν for varying flare angle θ. A variation in θ results in a considerable resonance frequency shift and change in effective area. As increasing values of θ correspond to a larger antenna area via Eq. (4.5) the effective area increases, as one would expect.

Attempts to establish an empirical relationship between A_{eff} and θ at the resonance frequency failed. Like with the previous simulations for varying values of l and l_{gap}, the value of the feed impedance was kept fixed at $Z_0 = 50\,\Omega$. However, the antenna impedance Z_A is a quantity that is heavily dependent on the flare angle of the antenna, as already established with Eq. (2.55) and Fig. 2.7 for a bow-tie antenna of infinite length. Under the assumption that a change in antenna impedance for a bow-tie antenna of finite length is predominantly caused by a variation in flare angle, it becomes evident that the impedance mismatch is significant when comparing values of the effective area for varying flare angle at fixed feed impedance, making a direct comparison difficult with the available data at hand.

Nonetheless, the value of θ should be maximized as much as possible, even under the assumption that the data obtained from the simulation is affected by an impedance mismatch.

4.2.1   Finalized Bow-tie Parametrization

Summarizing the results from the receiving scenario, it is evident that the antenna length should be matched to fit the desired resonance wavelength while cross-sectional area of the antenna should be maximized as much as possible by increasing the flare angle, with the gap length being minimized to the size of the sensing element. Due to geometrical limitations introduced by adjacent probing contacts near the antenna, which are required for the envisioned Hall bar structure of the sensing element, the maximum possible flare angle for the proposed antenna design in this thesis is $\theta = \pi/2$.

As an extension to Fig. 4.6 and to account for the significant shift in resonance frequency when varying the value of θ, the slope of the resonance wavelength versus the antenna length as in Fig. 4.11 has been calculated from the simulation data to allow for inter- and extrapolation of the required antenna length to match the desired resonance wavelength.

θ	slope	method
$1\pi/6$	2.961	direct
$2\pi/6$	3.340	fit
$3\pi/6$	3.807	direct
$4\pi/6$	4.441	direct
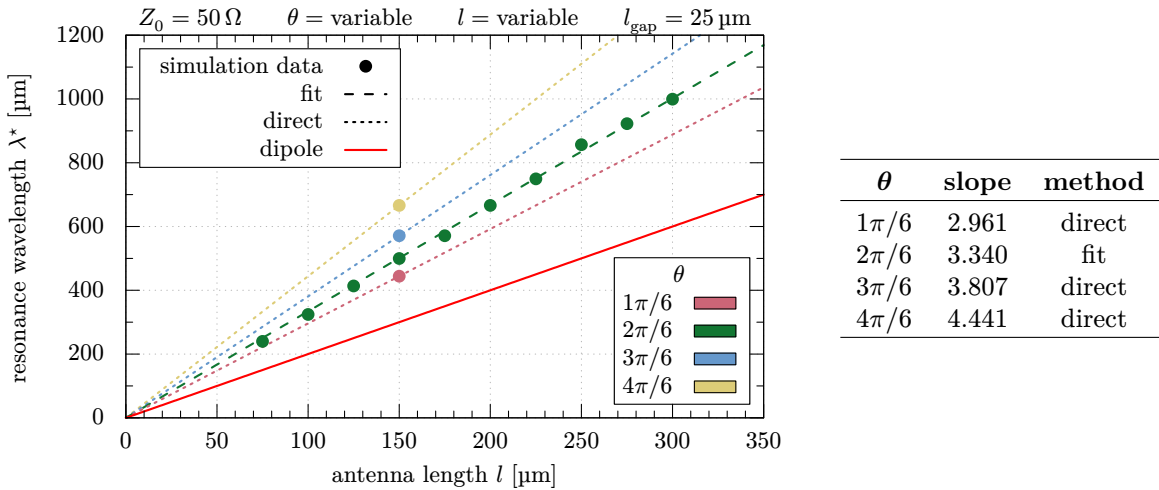
Figure 4.11: Plot of resonance wavelength $\lambda^\star$ versus antenna length l for varying values of θ. The data for $\theta = \pi/3$ is identical to that of Fig. 4.6 obtained via fitting, whereas the slope for all other values of θ has been calculated directly by the slope of the linear function intersecting the resonance position and origin of the graph.

For the desired resonance frequency of $\nu^\star = 0.5\,\text{THz}$ with corresponding resonance wavelength of $\lambda^\star \approx 599.6\,\mu\text{m}$, the corresponding length of the antenna should be equal to $l = 157.50\,\mu\text{m}$ at a fixed angle of $\theta = \pi/2$. As already established before, the gap length is kept at a value of $l_{\text{gap}} = 25\,\mu\text{m}$.

To confirm these results, the transmitting and receiving antenna model has been simulated for the calculated parameter values with an increased frequency resolution of $\Delta\nu = 0.01\,\text{THz}$. The results for the S_{11} parameter are visualized in Fig. 4.12.
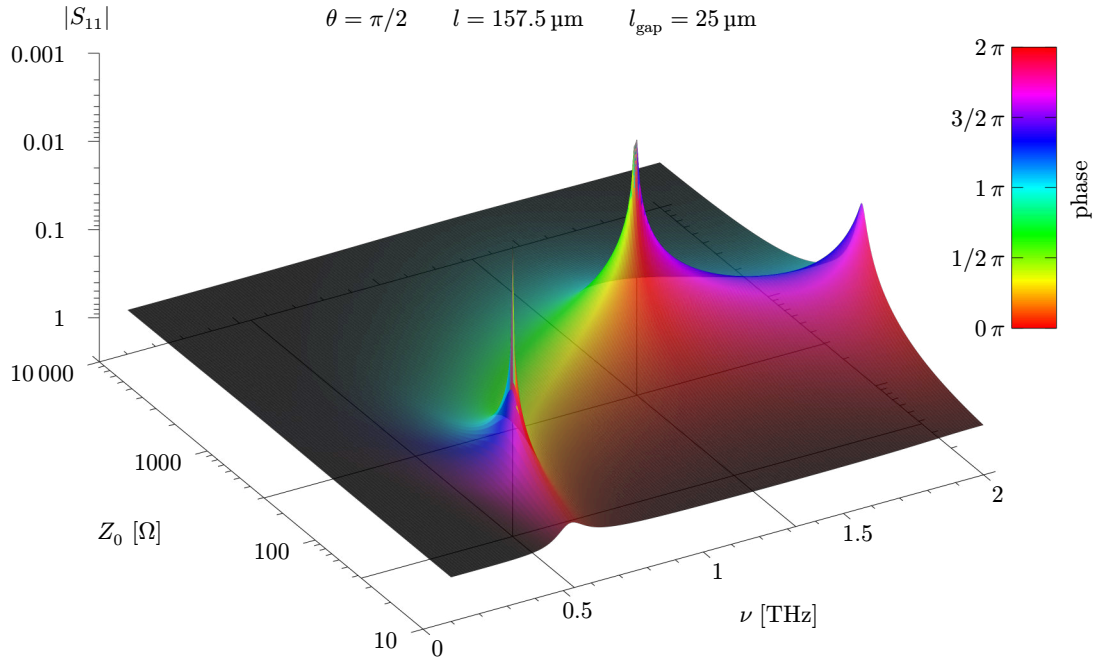
Figure 4.12: Surface plot of S_{11} versus frequency ν and feed impedance Z_0 with reversed z-axis. Similar to Fig. 4.1 multiple resonance peaks are visible, the first one being at roughly $\nu_1^\star \approx 0.54\,\mathrm{THz}$ with $Z_{A,1} \approx 37.5\,\Omega$, and the second peak at roughly $\nu_2^\star \approx 1.33\,\mathrm{THz}$ with $Z_{A,2} \approx 297.0\,\Omega$. Again, it is good practice to compare the resonance positions to the simulation data of the receiving model.

The simulation data for the receiving model at varying impedance is visualized in Fig. 4.13 and the power transfer at resonance in Fig. 4.14.
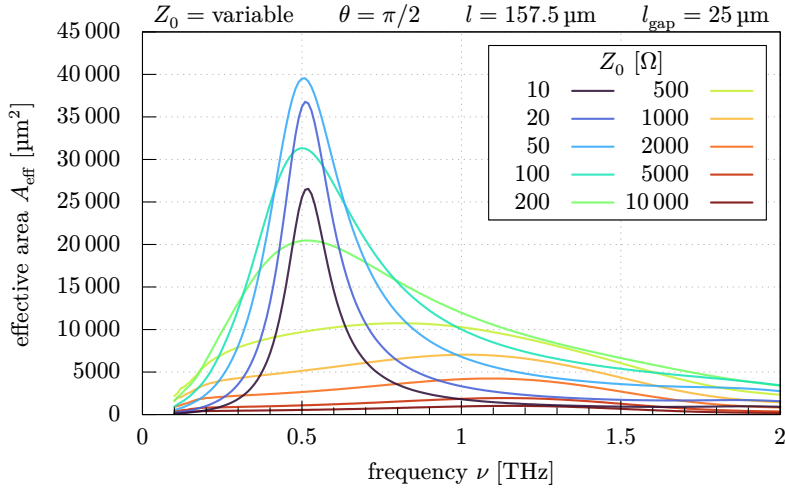
Figure 4.13: Plot of effective area A_{eff} versus frequency ν for varying feed impedance Z_0. Similar to the observation in Fig. 4.3, the effective area is maximal for a value of Z_0 between $20\,\Omega$ to $100\,\Omega$ at the apparent resonance frequency of $\nu^\star \approx 0.51\,\mathrm{THz}$.

The resonance frequency inferred from the receiving configuration is close to the desired value of $\nu^\star = 0.5\,\mathrm{THz}$, which demonstrates that the previously proposed design guidelines are functional for this specific case, and potentially also for an even wider parameter range within or outside the explored regime. The resonance frequency inferred from the transmitting configuration is somewhat different to the value obtained from the fit, possibly due to the reciprocity principle being not fulfilled entirely for both simulation configurations. To obtain a value for the antenna impedance, the fit procedure for the power delivery is repeated and visualized in Fig. 4.14 for the data at hand.

The antenna impedance inferred from both configurations is equal within the standard error
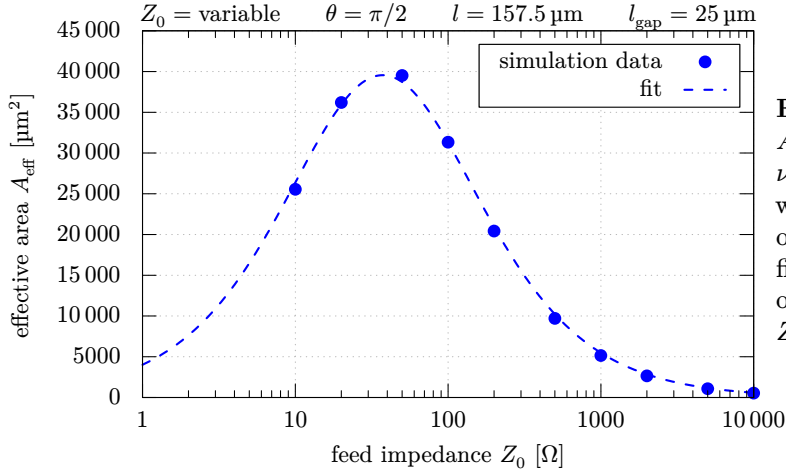
Figure 4.14: Plot of effective area A_{eff} versus feed impedance Z_0 at $\nu = 0.5\,\text{THz}$, fitted via Eq. (4.4), where $|V_A|$ and R_A are constants obtained through fitting. From the fit (with an R^2 value of 0.998), one obtains $|V_A| = (125.2 \pm 0.2)\,\mu\text{V}$ and $Z_A = (37.3 \pm 0.7)\,\Omega$.

obtained from the fit. Conclusively, both the transmitting and receiving configuration predict and confirm the desired resonance frequency of $\nu^\star = 0.5\,\text{THz}$. The antenna will therefore be fabricated with the parameter values established from the receiving configuration in Tab. 4.3.

parameter	$\nu^\star$	$\lambda^\star$	Z_A	l	l_{gap}	θ	d
value	$0.51\,\text{THz}$	$587.8\,\mu\text{m}$	$37.3\,\Omega$	$157.50\,\mu\text{m}$	$25\,\mu\text{m}$	$\pi/2$	$60\,\text{nm}$

Table 4.3: Parameter configuration for the final antenna design. The value for Z_A corresponds to the antenna impedance inferred at $\nu = 0.5\,\text{THz}$, which is close to the actual resonance frequency inferred from the data in Fig. 4.13.

At last, the compatibility of the antenna with a circularly polarized source is discussed. So far, the receiving configuration assumed the incident plane wave to be polarized at 0° angle, however the photomixer utilized in the experiment emits circularly polarized terahertz radiation. A sanity check is therefore required to confirm the compatibility of the antenna with the experimental setup. The simulation for the final parameter configuration was repeated for four different Jones vectors to study the change in effective area. The amplitude was kept constant at a value of $|\mathbf{E_0}| = E_0 = 1\,\text{V m}^{-1}$ for all polarization directions:

$$\mathbf{E_{0,0°}} = E_0 \begin{pmatrix} 1 \\ 0 \end{pmatrix} \qquad (4.9)$$

$$\mathbf{E_{0,45°}} = \frac{E_0}{\sqrt{2}} \begin{pmatrix} 1 \\ 1 \end{pmatrix} \qquad (4.11)$$

$$\mathbf{E_{0,90°}} = E_0 \begin{pmatrix} 0 \\ 1 \end{pmatrix} \qquad (4.10)$$

$$\mathbf{E_{0,\text{circ}}} = \frac{E_0}{\sqrt{2}} \begin{pmatrix} 1 \\ \pm i \end{pmatrix} \qquad (4.12)$$

Due to symmetry considerations of the model, it is not necessary to distinguish between left-handed and right-handed circular polarization. The choice of the sign in Eq. (4.12) is therefore arbitrary and leaves the resulting values for the effective area invariant. The receiving model has been simulated at a decreased frequency resolution of $\Delta\nu = 0.025\,\text{THz}$, with the resulting data being visualized in Fig. 4.15.

Conclusively, no adjustments to the polarization are required, at cost of half the delivered power.

In order to compare the simulation results of this thesis to those of other papers, the electric near-field enhancement by the receiving bow-tie antenna proves to be an excellent method to validate the simulation model.

To validate the receiving bow-tie model employed within the thesis, the electric near-field enhancement can be compared to the results of other papers. The resulting data in Fig. 4.16 has been obtained by simulating the receiving antenna model with the lumped port feature disabled. Additionally, the distance between the antenna and perfectly matched layer has been doubled, the error margins
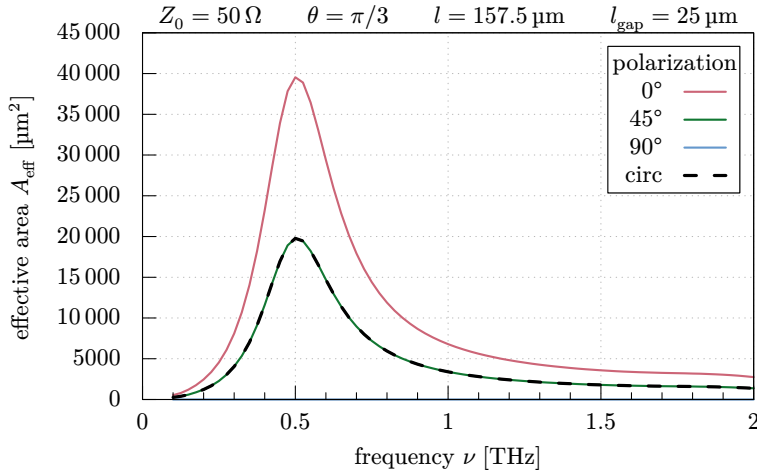
Figure 4.15: Plot of effective area A_{eff} versus frequency ν for varying polarizations. Notably, there is no delivered power for a perpendicular polarization of 0° and the delivered power for a 45° and circularly polarized wave are equal. These results suggest, that only the E_{0x} component contributes to the power delivery of the simulated bow-tie antenna configuration.

improved to a value of 0.001, the minimal size of gap's mapped mesh decreased to a size of $\lambda/750$, and the minimal mesh size of the antenna's mapped mesh decreased further to $\lambda/200$ in order to increase the resolution and accuracy of the simulation as much as possible for the computer hardware at hand.
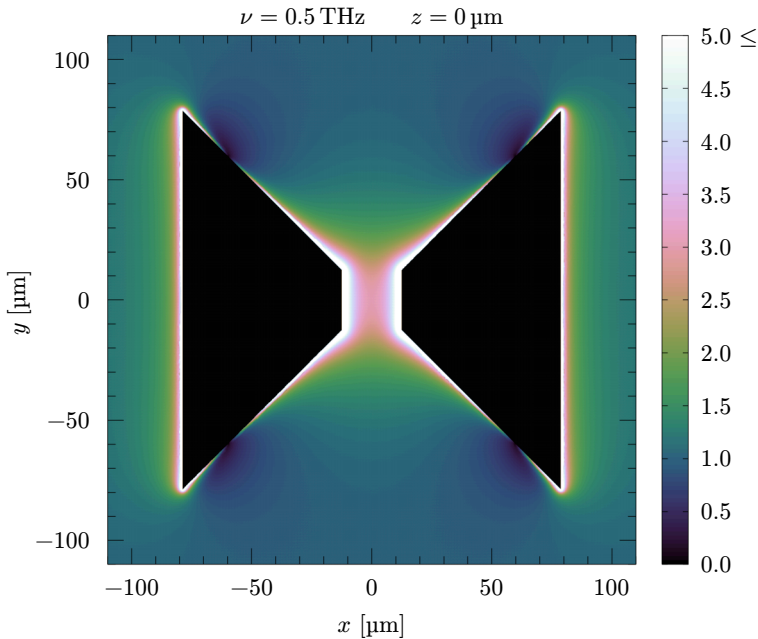
Figure 4.16: Relative near-field enhancement of the electric field's phasor for the finalized bow-tie antenna in the xy-plane. The electromagnetic fields inside a perfect electric conductor are an undefined quantity within *COMSOL* and are therefore drawn black.

This concludes the simulation procedure, with only the discussion of the results and fabrication process remaining.

4.3 Discussion of Results

As this thesis is unable to provide measurements for the antenna's predicted properties, it is required to carefully compare the obtained results with those of other papers relying on simulation data.

Gonzalez et al. [8] compared four different antenna designs in a receiving configuration via simulations using *COMSOL* as in Fig. 4.17a and observed that the electric field enhancement at the antenna feed of the bow-tie antenna was more than twice as large compared to the other studied antenna designs. Additionally, the resonance frequency of 1.35 THz (which corresponds to a free-space wavelength of 222 µm) observed for their bow-tie antenna with $l = 80\,\mu\text{m}$ and unspecified flare angle, inferred from Fig. 4.17a, lies within 0.15 THz of the value predicted by the linear proportionality of the resonance

wavelength to antenna length as in Fig. 4.11 for a bow-tie antenna of length $l = 80\,\mu\text{m}$ and flare angle of $\theta = \pi/6$.

The solidity of the employed simulation model employed is validated further by the comparison of the electric near-field enhancement computed in this thesis with the results of Runge et al. [33] as in Fig. 4.17b, who calculated the spatial distribution of the electric field for a bow-tie antenna.

(a)   different antenna designs

(b)   electric near-field enhancement
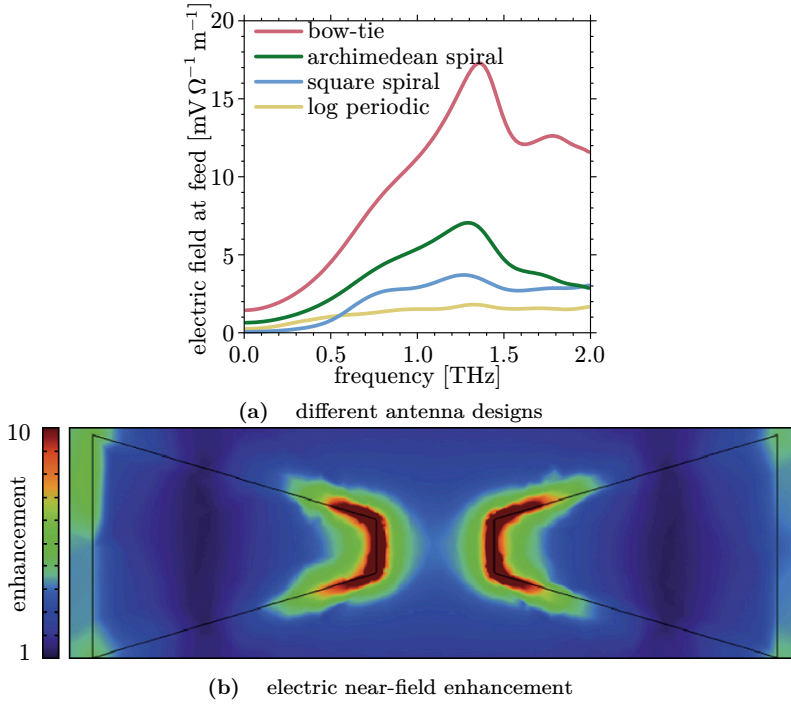
Figure 4.17: (a) Plot of the electric field at the antenna feed versus frequency for four different antenna geometries. The resonance position of the bow-tie antenna with a length of $l = 80\,\mu\text{m}$ and negligible gap size by Gonzalez et al. aligns well with the resonance frequency for the effective area observed in this thesis in Fig. 4.5. Adapted from [8, fig. 1 center]. (b) Electric near-field enhancement of the bow-tie antenna by Runge et al. with a single lobe length of $53\,\mu\text{m}$ and gap length of $22\,\mu\text{m}$. The features of the electric field distribution near the edges of the antenna are well preserved and quite similar to the profile visualized in Fig. 4.16 for the data obtained in this thesis. Adapted from [33, fig. 5a].

Furthermore, it would be beneficial to outline differences for the antenna design of this thesis compared to the designs that were commonly proposed to similar experiments, as the antenna's properties of interest are heavily dependent on the geometry of the design.

The terahertz detector proposed by Vicarelli et al. [6] utilizes a circular-toothed log-periodic antenna as in Fig. 1.1a, which is also attuned to linearly polarized radiation and exhibits multiple resonance frequencies close to each other in the lower terahertz range. The bow-tie antenna design explored in this thesis is more or less a geometrical derivative of a dipole antenna and should therefore also have resonances at integer multiples of $\lambda/2$ for negligible gap sizes, as argued before in Sec. 2.2.3. The sending configuration of the antenna did indeed predict multiple resonance frequencies, which aligns with the observations of Viti et al. [7] for a rounded antenna design. It should however be emphasized that careful investigation regarding the higher-order resonances is required when trying to deduce the suitability of these apparent resonances for the experimental setup at hand, which is why this thesis limited the interpretation and analysis to the first resonance frequency $\nu_1^\star$ only.

If the antenna should be attuned to circularly polarized radiation, a spiral-shaped antenna might be more appropriate to begin with [8, 34]. Nonetheless, the results for the polarization dependence of the antenna design proposed in this thesis suggest that a bow-tie antenna can, at cost of half the delivered power, be used in combination with circularly instead of linearly polarized light (see Fig. 4.15).

Regardless of the utilized antenna design, the impedance mismatch between antenna and sensing element is a significant problem as the antenna impedance for the investigated design does not easily

exceed the lower hundreds of ohms for each lowest observed resonance frequency. This impedance mismatching issue aligns with what other papers reported in that regard and remains to be a problem that remains yet to be solved. [9, 10, 34]

It is important to note that this thesis did not consider any material properties for the simulation model, which requires careful interpretation of the results when employing the established guidelines for the design and fabrication of a bow-tie antenna for the use case outlined in Sec. 1. The dielectric properties of the substrate can change the propagation speed of currents on the antenna's surface and introduce shifts in the resonance frequencies, which was not investigated during the simulation process of this thesis. [35]

Additionally, the electrical antenna and probing contacts were not considered during the simulation. Due to their perpendicular placement in the lithography pattern introduced in Sec. 5.1, they are expected to have no meaningful impact on the antenna's response behavior for incident radiation with linear polarization along the x-axis. This hypothesis was not tested and cannot be applied to the case of circularly polarized radiation.

4.3.1 Outlook

Throughout the whole study process it was apparent that computational processing power was the main limiting factor, which prevented a thorough exploration of the model beyond the employed configuration and investigated geometrical degrees of freedom. With the available computer hardware, the simulation time of the reduced model was generally between 5 min to 60 min, whereas the full model (depending on the varying parameters) generally took between 2 h to 8 h to simulate, with some high-resolution models even exceeding computation times of several days. This lack of time prevented the exploration of other effects, such as the ones mentioned in Sec. 4.3.

Attempts have been made to reduce the simulation model into a two-dimensional problem, which would have drastically reduced the computational complexity and therefore also the processing time, but ultimately failed to yield results similar to those of the three dimensional model, due to limitations of the lumped port feature used within *COMSOL*. Moreover, only few degrees of freedom have been changed at a time to keep the model predictable and avoid misleading conclusions when changing too many degrees of freedom at once.

Conclusively, due to the outlined limitations and simplifications of the physical model, careful interpretation is required when applying the results obtained from the simulations to the real experimental setup. Nonetheless, trends in the data have been established successfully which should prove to be useful when adapting the model to more specific configurations of the real physics at work. Ultimately, real experimental measurements are required to confirm or contradict the established design and fabrication guidelines for the proposed bow-tie antenna design.

5 Fabrication

The antenna is to be fabricated on 4-inch prime grade silicon wafers with a $285\,\mathrm{nm}$ ($\pm 5\,\%$) thick non-conductive layer of thermal oxide as a substrate. The wafers are $\{1\,0\,0\}$ p-type wafers, with boron used as a dopant, a thickness of $(525 \pm 25)\,\mathrm{\mu m}$, and resistivity of $< 5\,\mathrm{m\Omega\,cm}$.

Similar to the fabrication process utilized in Wang et al. [26], the antenna was, after patterning the substrate via photolithography, evaporated onto the substrate via electron-beam evaporation of chromium and gold. The antenna was processed within a clean room to minimize any defects of the fabricated devices caused by potential particle contamination. The fabrication process of the antenna is described up until the lift-off process in acetone. The finalized device, as it is required for the experimental setup in Sec. 1, requires additional processing steps such as the stacking of hBN and graphene monolayers to build the sensing element, electron-beam lithography for evaporation of the electrical contacts, and the process of wire bonding the fabricated sample onto PCB, which is not covered in this thesis.

5.1 Lithography Pattern

The lithography pattern for the antenna, shown in Fig. 5.1, was created via the open-source mask viewing and editing software *KLayout* [36]. Besides the antenna itself, there are various support structures and additional probing contacts positioned perpendicular to the antenna along the *y*-axis, which in turn are connected to contact pads that are necessary for wire bonding of the electrical contacts. Furthermore, the mask is labeled with the resonance frequency and geometrical parameters to allow for quick identification of the antenna with a regular light microscope. Towards the top of the mask, a notch that is visible to the naked eye and additional alignment crosses are placed to help with the alignment process during electron beam lithography. The shape of the antenna contacts has been inspired from the terahertz bow-tie antenna design utilized in Liu et al. [37].

5.2 Sample Preparation

5.2.1 Wafer Cleaving

The first step of the fabrication process is the cleaving of the silicon wafer into smaller pieces using the utilities shown in Fig. 5.2a. This process can be omitted when the wafer is processed as a whole.
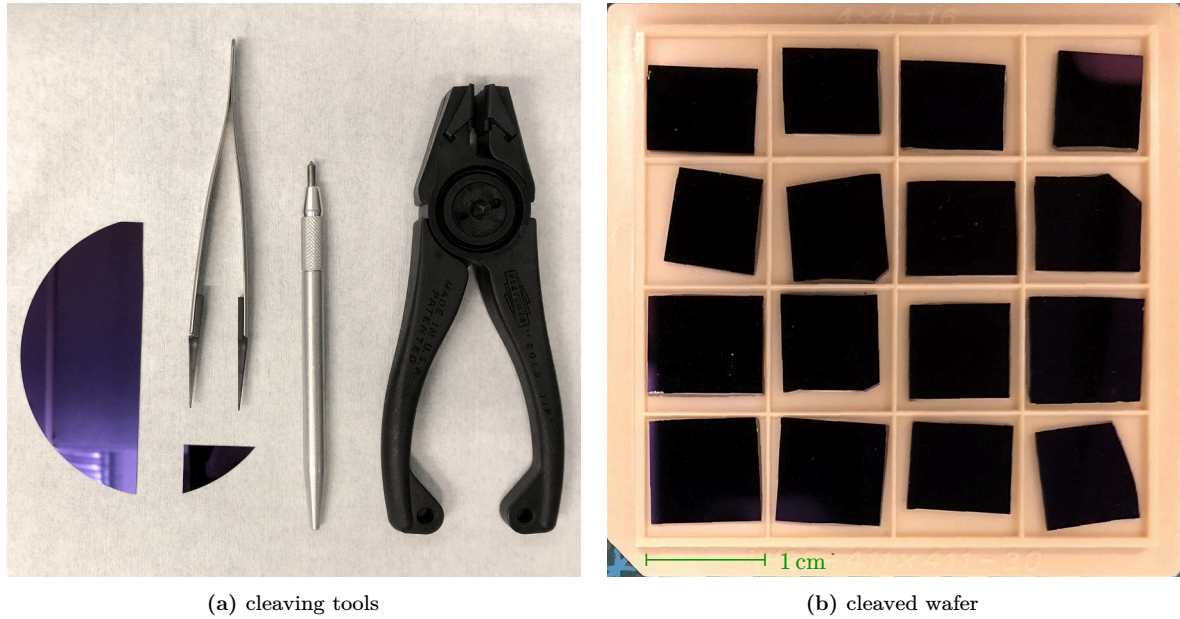
At first, the wafer was lightly scored perpendicular to the primary and secondary flats with a diamond scribe at the desired position of the break. The wafer breaks clean at the marked position by applying little force to this spot via wafer cleaving pliers. It is beneficial to do this process as accurate as possible to prevent the formation of uneven side walls, which reduce proper contact between pliers and the edges of the smaller wafer pieces and increase the risk of accidentally dropping them. The prepared pieces are stored and transported inside a waffle pack die tray as in Fig. 5.2b.

5.2.2 Substrate Cleaning

It is of utmost importance to thoroughly clean the wafer pieces before the next fabrication steps to remove or reduce any potentially preexisting contamination of the substrate, especially after breaking the wafer because of small wafer particles that are created with every break during the cleaving process. Contaminated samples are more likely to have defects or inhomogeneities in the photoresist layer after spin coating. Acetone and isopropyl alcohol were used as cleaning agents, therefore appropriate safety measures have to be taken when handling these chemicals [38, 39]. The results obtained from rinsing the small pieces with acetone and isopropyl alcohol alone were unsatisfactory.

Figure 5.1: Photomask of the finalized antenna design, with a total size of 4800 μm × 4800 μm, and annotations to various features of the mask. A magnified view of the label and antenna itself are provided in the green areas to improve visibility of smaller features of interest. The contact pads are individually numbered and consist of three connected pads, with two of them acting as a reserve in case of wire bonds that accidentally break through the insulating oxide layer of the substrate, which is detrimental for devices that rely on using silicon as back gate.

(a) cleaving tools

(b) cleaved wafer

Figure 5.2: Setup and tools used for manual wafer cleaving. (a) From left to right: partially cleaved silicon wafer, tweezers with carbon fiber tip, diamond scribe, wafer cleaving pliers. (b) Roughly square-shaped wafer pieces after cleaving with a size of $\sim 1\,cm^2$.

Optimal results have been achieved by sonication of the samples inside a bath of acetone for 5 minutes at 50 °C followed by a bath of isopropyl alcohol at the same time and temperature. To remove any liquid residuals, the samples have been blow-dried with a nitrogen spray gun. A before-and-after comparison of the cleaned samples is provided in Fig. 5.3.

(a) before cleaning
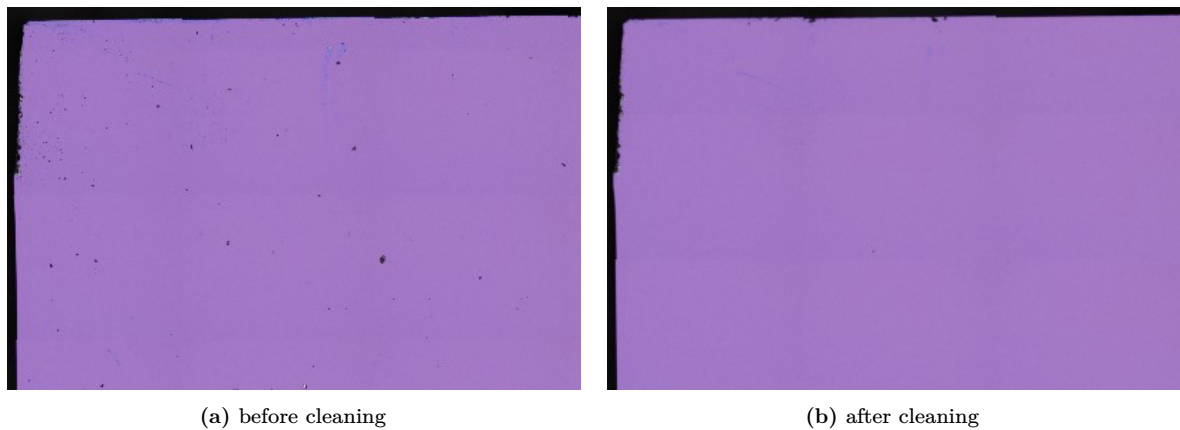
(b) after cleaning

Figure 5.3: Microscopic image of a wafer sample's surface near the substrate's corner. (a) Sample directly after cleaving. (b) Sample after sonication in acetone and isopropyl alcohol.

5.3   Photolithography

5.3.1   Spin Coating

After sufficient cleaning, the samples are first spin coated with a layer of 10 % hexamethyldisilazane diluted with isopropyl alcohol and baked to promote adhesion between the photoresist and silicon substrate [40]. The hexamethyldisilazane was spin coated at 6000 revolutions per minute for 60 seconds with an acceleration of $2000\,s^{-2}$ and subsequently baked on a hotplate for 1 minute at 100 °C. It is possible to omit the process of spin coating hexamethyldisilazane onto the substrate,

however, this results in the photoresist tending to be more brittle at the edges of the substrate after development. This is not necessarily detrimental to the to-be-fabricated device but can induce other defects or inhomogeneities to the photoresist layer. Subsequently, all substrates were coated with hexamethyldisilazane and baked to avoid the described defects.

The process is continued by spin coating AZ 5214 E photoresist onto the samples at 6000 revolutions per minute for 40 seconds with an acceleration of $2000\,\mathrm{s^{-2}}$. The chosen rotational speed produces a film thickness of roughly $1.14\,\mathrm{\mu m}$ as inferred from the product data sheet [41]. Right after coating the sample is baked on a hotplate at $100\,^{\circ}\mathrm{C}$ for 1 minute, below the critical temperature for image reversal baking for the chosen photoresist. This configuration ensures that the photoresist layer is a positive image of the mask pattern.

The quality of the photoresist film is heavily dependent on the cleanliness of the sample before spin coating. Ideally, the layer is homogeneous in the center with no visible defects, such as the sample depicted in Fig. 5.4a. Contamination or inhomogeneities of the photoresist layer, such as the one in Fig. 5.4b are the undesirable result caused by insufficient cleaning.

(a) no visible defects   **(b)** visible contamination
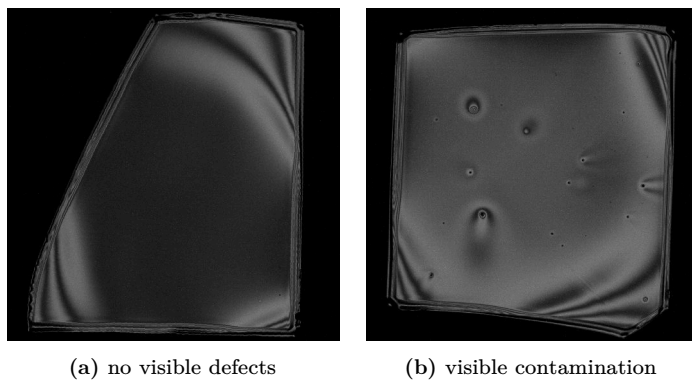
Figure 5.4: Microscopic image of the wafer sample's surface after spin coating photoresist, with visible thin-film interference patterns near the edge of the substrate due to varying film thickness. (a) The photoresist thickness in the center of the substrate is homogeneous and ideal for photolithography. (b) The area of interest in the center of the substrate is visibly contaminated by residuals particles, leaving no suitable area for photolithography.

5.3.2 Exposure and Development

From this point on, the samples should no longer be exposed to ultraviolet light in an uncontrolled manner. The utilized photoresist is spectrally sensitive in a range of $310\,\mathrm{nm}$ to $420\,\mathrm{nm}$ and illuminated by a $365\,\mathrm{nm}$ LED during the exposure process. In order to choose the optimal dose and optical defocus settings for the exposure of the finalized pattern in Sec. 5.1, the lithography process was optimized by studying an exposure series for the different values of dose and defocus listed in Tab. 5.1 for the test design in Fig. 5.5.

parameter		optimal	start	end	step
dose	$[\mathrm{mJ\,cm^{-2}}]$	200	100	400	25
defocus	[%]	20	0	40	5

Table 5.1: Table of the settings used for the exposure series with optical defocusing. The column titled 'optimal' refers to the values which resulted in the best image quality.

Both available metal ion free developers, AZ 726 MIF and AZ 826 MIF, are compatible with the used photoresist. The latter one was chosen due to the visibly improved quality of small features compared to the former [42]. The samples were developed by submerging them completely into the developer for 45 seconds, which is enough time to develop the exposed sample completely, and subsequently washed in deionized water to halt the development process. If there are still some developer or photoresist residuals left after 45 seconds, the sample can be developed for an additional 5 to 10 seconds to remove
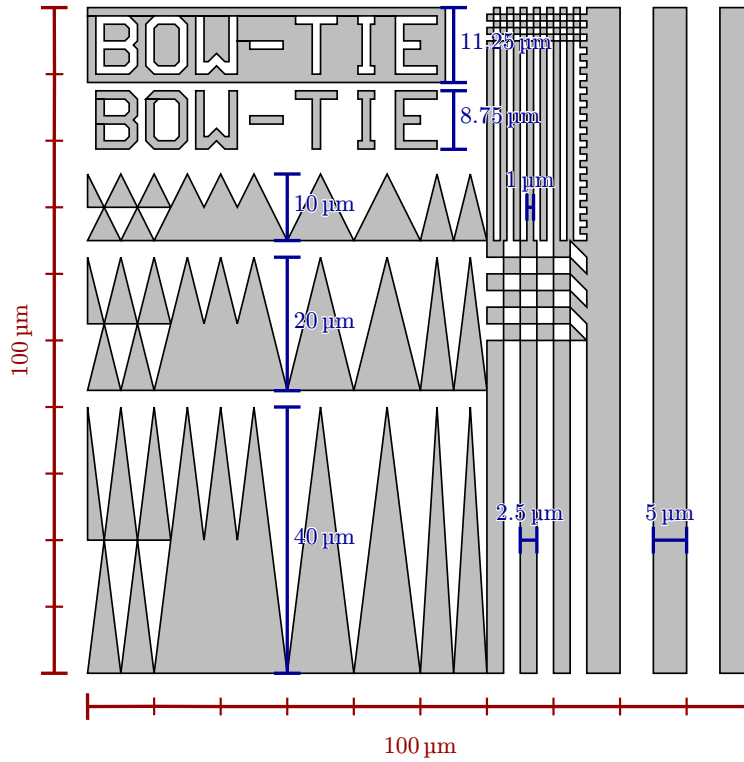
Figure 5.5: Test mask for the exposure series with feature sizes down to 1 µm². To push the photolithography to its limits, features of different sizes are embedded into this compact 100 µm × 100 µm design to be able to identify the best settings. The probing contacts of the design presented in Sec. 5.1 have a line width of 5 µm with the smallest feature size being the central alignment markers with a line width of 1 µm.

the unwanted remainders. The exposure series indicated the best settings to be a dose of $200 \, \text{mJ cm}^{-2}$ and optical defocus of 20 %. A comparison of the developed test structure is shown in Fig. 5.6.

(a) dose $200 \, \text{mJ cm}^{-2}$, defocus 20 %   **(b)** dose $200 \, \text{mJ cm}^{-2}$, defocus 0 %   **(c)** dose $300 \, \text{mJ cm}^{-2}$, defocus 20 %
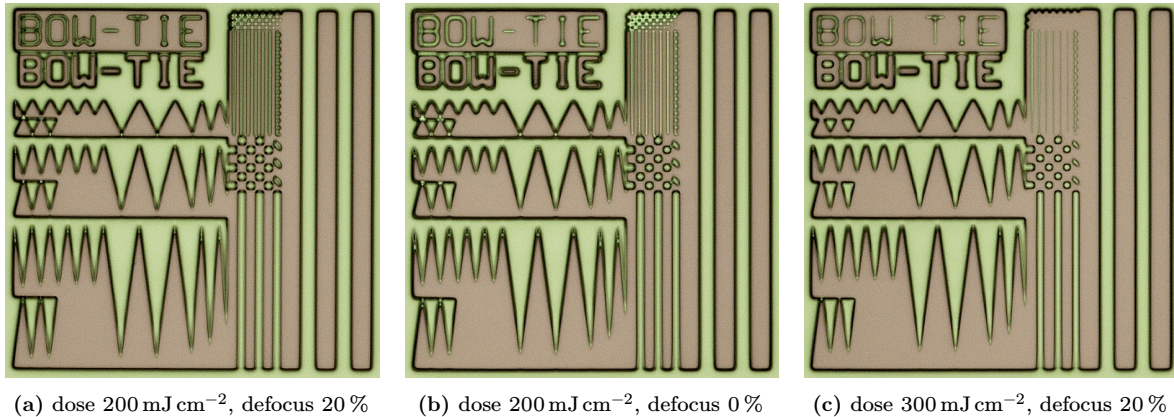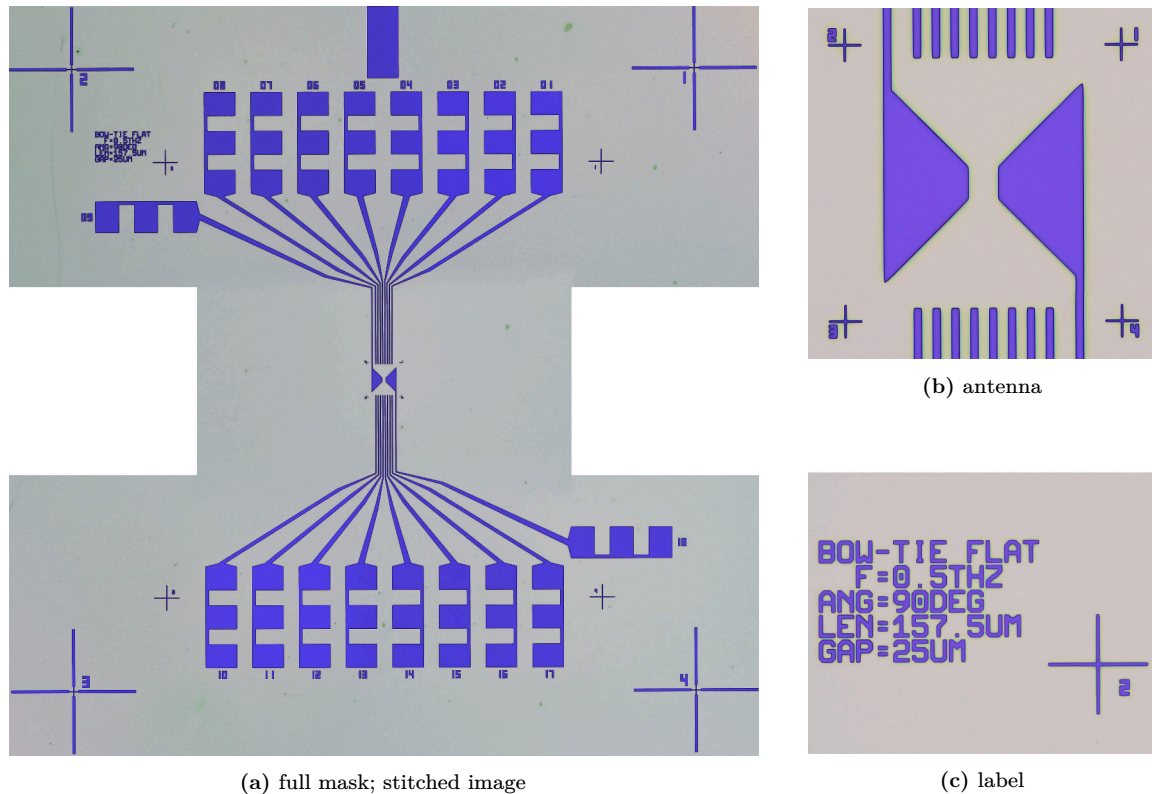
Figure 5.6: Microscopic image of the test pattern's exposure series for various values of dose and optical defocus, developed with AZ 826 MIF. (a) Fully developed photoresist with good results for both quality and preservation of small and sharp features. (b) Unsuitable values for the defocus result in dull corners of sharp, pointy structures and quality loss of small features. (c) Overexposure results in removal of the photoresist film during development beyond the feature's boundaries defined by the photomask, completely eradicating small structures in the process.

Accordingly with the exposure series' results, yielding optimal image quality for a dose of $200 \, \text{mJ cm}^{-2}$ and optical defocus of 20 %, the samples were exposed with the finalized antenna pattern as a mask. The image quality was, as expected, satisfactory in combination with the previously mentioned settings in combination with AZ 826 MIF as a developer. Microscopic images of the developed samples are shown in Fig. 5.7. It is nonetheless possible (and required when using the same type of photoresist from different storage conditions or fabrication batches) to vary the exposure dose for fine tuning of the image quality, as the results can be quite different when variations are introduced

to the fabrication process outside of the extent as outlined throughout the thesis. It is good practice to conduct one or more exposure series when in doubt to avoid unfavorable results during lift-off.


(a) full mask; stitched image

(b) antenna

(c) label

Figure 5.7: Microscopic image of the antenna's fully developed lithography pattern from Sec. 5.1. (a) Stitched image of the whole pattern. (b) Close-up of the bow-tie antenna, including the end of the probing contacts, which have to be connected to the sensing element via electron-beam lithography. (c) Close-up of the label. The developed image has no visual defects, which validates the used exposure settings.

5.4 Evaporation and Lift-off

For evaporation, the samples were secured onto the substrate holder using Kapton tape as in Fig. 5.8a before being secured properly inside the load lock of the ultra-high vacuum electron-beam evaporator. By the principle of electron-beam vapor deposition, the to-be-deposited material is exposed to electrons accelerated by high voltage in the kilovolts range, evaporating the material on impact. The film thickness is monitored by a quartz crystal microbalance, which relies on the change in frequency of the quartz crystal resonator upon a change in the deposited mass to measure the deposited layer thickness with high precision.

First, a 5 nm thick layer of chromium was evaporated on the loaded samples in order to improve adhesion between the gold film and silicon substrate. An electron current of 23 mA resulted in a deposition rate of $\sim 0.06\,\mathrm{nm\,s^{-1}}$. The process was repeated for the 55 nm thick layer of gold, for which a current of 65 mA resulted in a deposition rate of $\sim 0.07\,\mathrm{nm\,s^{-1}}$. The pressure inside the chamber can range from $\sim 10^{-6}$ mbar down to $\sim 10^{-8}$ mbar during the evaporation process. The samples after unloading are shown in Fig. 5.8b.

For the lift-off procedure, the samples were placed in a glass beaker containing acetone held at 60 °C by a hot plate to remove the photoresist from the substrate, which carries the excess metal film that needs to be removed in order to reproduce the to-be-manufactured design from Sec. 5.1. The
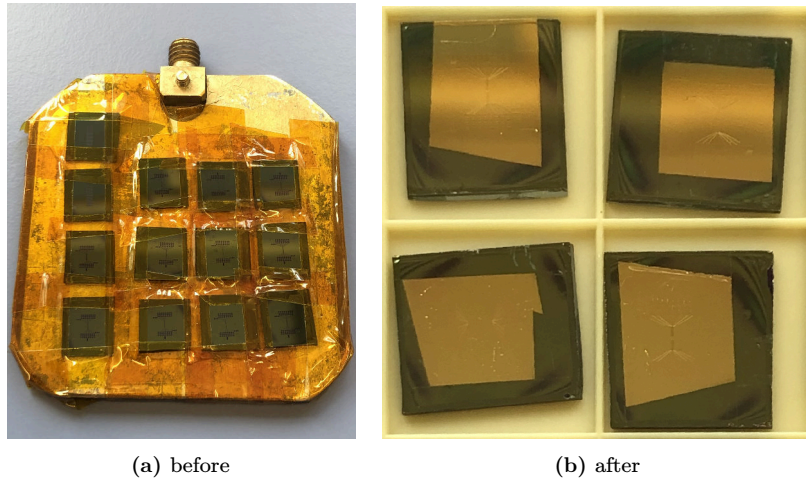
(a) before

(b) after

Figure 5.8: Samples before and after the evaporation process. The samples are fixated onto the substrate holder which in turn is threaded onto a magnetically coupled linear transfer stage to move the holder from the load lock into the evaporation chamber. All that is left to do after evaporation is the lift-off procedure to remove the excess metal film from the substrate.

boiling point of acetone is at approximately 56 °C, the beaker was therefore covered with aluminum foil to prevent the acetone from evaporating completely, which would be detrimental to the fabricated antenna. For a total amount of three times, the acetone was renewed periodically in one-hour intervals. At each renewal, it was attempted to remove the excess chromium-gold layer by using an acetone-filled syringe to wash off the film and minimize the risk of retention. During the whole process, the samples have to be submerged completely in the acetone to prevent redeposition of the metal film back on the substrate.

After lift-off, the samples were washed with isopropyl alcohol and blow-dried using a nitrogen spray gun to remove any unwanted residuals of the film and acetone. No visual defects that could impact the function of the device have been identified. On the edges of the metal layer, some photoresist residuals did not solve completely, shown in Fig. 5.9.


Figure 5.9: Non-detrimental residuals of the photoresist film near the edges of the metal layer. Although they are visually unpleasing and can be mistaken for breaks in the contacts, this cosmetic defect does not impact the functionality of the device, as all contacts are electrically intact.

Although the small residuals should not negatively impact the function of the fabricated antenna, the affected samples were placed back into a beaker filled with acetone and sonicated for 1 minute at 50 °C. Sonication managed to remove most of the residual photoresist, but did in a few cases damage the fabricated device, sometimes even detrimentally, as shown in Fig. 5.10. The sonicator should therefore only be used if the defects impact the function of the device negatively and not for cosmetic issues like the one shown in Fig. 5.9.

Better results might be possible by utilizing the image reversal capabilities of the used photoresist, which would result in a slope profile with considerable overhang at the boundaries of the photoresist film, which would be better suited for lift-off [41]. Due to a lack of time, it was not possible to explore this option during the photolithography procedure.

Microscopic images of the finalized antennas are provided in Fig. 5.11, which concludes the fabrication process to the extent, as it is outlined in this thesis.

(a) nondetrimental

(b) detrimental
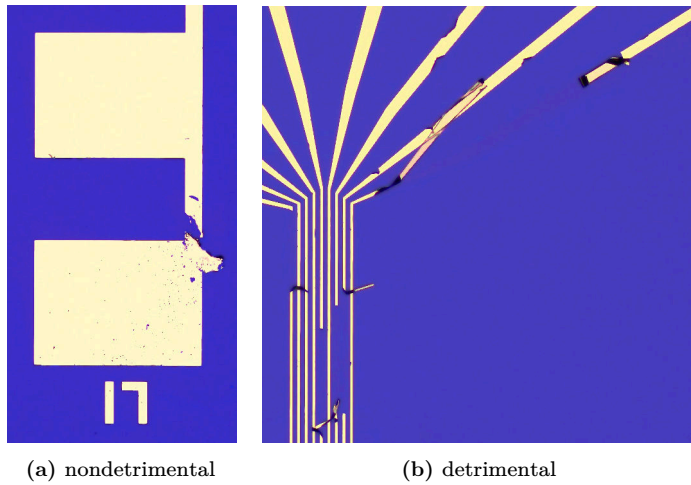
Figure 5.10: Microscopic image of possible visual damage after sonication. (a) The contact between one spare contact pad and the remaining structure is broken, which does not render the device unusable. (b) The probing contacts were lifted off the substrate during of the sonication process, rendering the device dysfunctional.

(a) full mask; stitched image
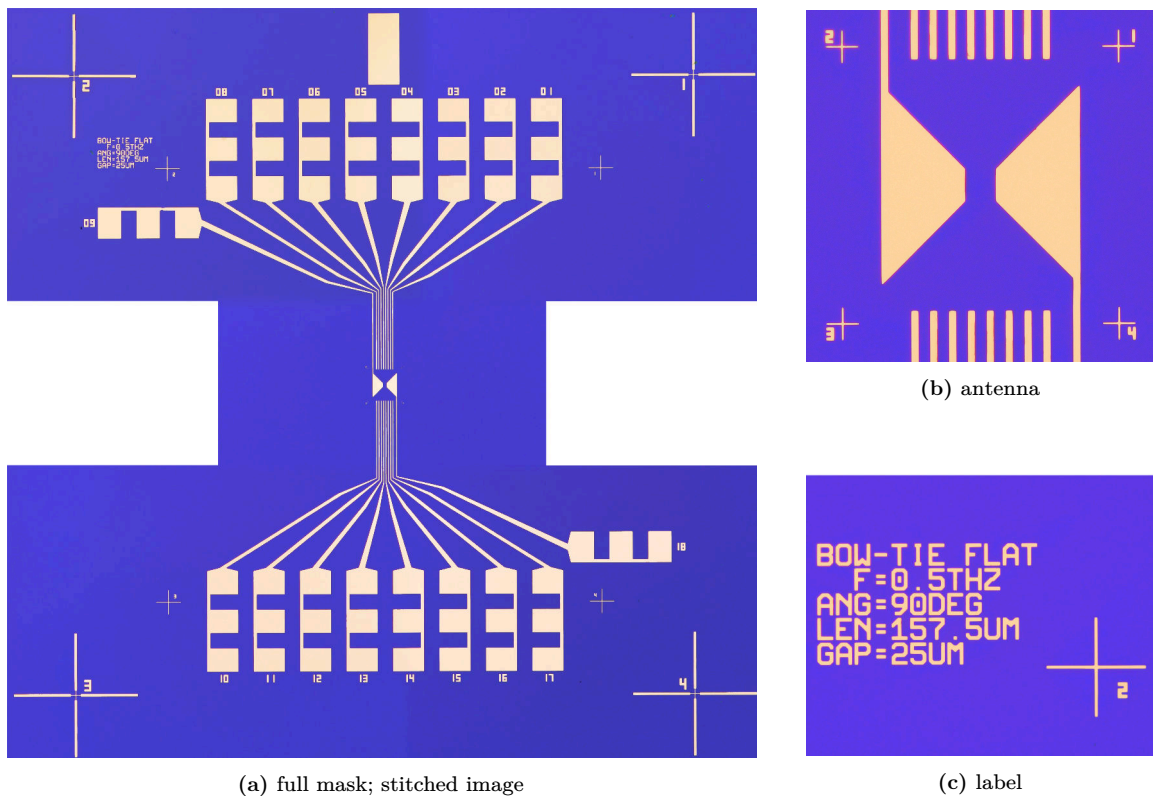
(b) antenna

(c) label

Figure 5.11: Microscopic image of the antenna's fully evaporated pattern. (a) Stitched image of the whole pattern. (b) Close-up of the bow-tie antenna. (c) Close-up of the label. All features of interest are preserved with exceptional quality with no superficial defects being visible, further validating the used exposure settings' correctness and overall fabrication process.

6   Conclusion and Outlook

The goal of this thesis was to establish design and fabrication guidelines for bow-tie antennas resonant in the terahertz range for their application in novel detector technology for terahertz radiation utilizing the unique band structure properties of moiré materials. These guidelines have been established successfully with the help of finite element simulations of a reduced model. The employed model did not account for any material properties or physical effects introduced by anisotripies and non-linearities in the geometry or physical interactions. It was not possible to mitigate losses caused by the impedance mismatch between the antenna and sensing element of the detector. From the resulting data it was possible to predict a geometrical parameter combination for a bow-tie antenna with resonance at 0.5 THz, which was confirmed by subsequent simulation of the mentioned model for the newfound parameters properties. The antenna has been successfully fabricated on silicon as a substrate by utilizing photolithography and thin-film deposition of gold via electron-beam evaporation.

Nonetheless, careful interpretation is required when adapting the presented simulation model for variations of terahertz detection experiments due to the disregarded material effects of the substrate and sensing element, at least until experimental confirmation or invalidation of the predicted antenna properties is provided. The employed analysis methodology based on RF engineering fundamentals can prove to be useful beyond the design and fabrication of a bow-tie antenna for terahertz detection purposes. Further refinements of the model are possible to explore cause and effect of other parameters and degrees of freedom, such as antenna thickness or the dielectric and anisotropic properties of the substrate, which were not explored in the scope of this thesis.

Bibliography

[1] L. Viti and M. S. Vitiello, "Tailored nano-electronics and photonics with two-dimensional materials at terahertz frequencies," Journal of Applied Physics **130**, 170903 (2021).

[2] L. Du, M. R. Molas, Z. Huang, G. Zhang, F. Wang, and Z. Sun, "Moiré photonics and optoelectronics," Science **379**, eadg0014 (2023).

[3] G. Di Battista, P. Seifert, K. Watanabe, T. Taniguchi, K. C. Fong, A. Principi, and D. K. Efetov, "Revealing the Thermal Properties of Superconducting Magic-Angle Twisted Bilayer Graphene," en, Nano Letters **22**, 6465–6470 (2022).

[4] G. Di Battista, K. C. Fong, A. Díez-Carlón, K. Watanabe, T. Taniguchi, and D. K. Efetov, "Ultra-low carrier density superconducting bolometers with single photon sensitivity based on magic-angle twisted bilayer graphene," en, arXiv:2403.02049 [cond-mat.mes-hall], 10.48550/arXiv.2403.02049 (2024).

[5] P. Seifert, X. Lu, P. Stepanov, J. R. Durán Retamal, J. N. Moore, K.-C. Fong, A. Principi, and D. K. Efetov, "Magic-Angle Bilayer Graphene Nanocalorimeters: Toward Broadband, Energy-Resolving Single Photon Detection," Nano Letters **20**, 3459–3464 (2020).

[6] L. Vicarelli, M. S. Vitiello, D. Coquillat, A. Lombardo, A. C. Ferrari, W. Knap, M. Polini, V. Pellegrini, and A. Tredicucci, "Graphene field-effect transistors as room-temperature terahertz detectors," Nature Materials **11**, 865–871 (2012).

[7] L. Viti, D. G. Purdie, A. Lombardo, A. C. Ferrari, and M. S. Vitiello, "HBN-Encapsulated, Graphene-based, Room-temperature Terahertz Receivers, with High Speed and Low Noise," Nano Letters **20**, 3169–3177 (2020).

[8] F. J. Gonzalez, M. S. Lodge, M. Ishigami, R. A. Klemm, A. Rathod, K. L. Lina, A. C. Bowman, F. Hernandez, C. J. Fredricksen, C. Cariker, and R. E. Peale, "Antenna-coupled graphene josephson-junction terahertz detector," MRS Advances **8**, 148–151 (2023).

[9] M. Kravtsov, A. L. Shilov, Y. Yang, T. Pryadilin, M. A. Kashchenko, O. Popova, M. Titova, D. Voropaev, Y. Wang, K. Shein, I. Gayduchenko, G. N. Goltsman, M. Lukianov, A. Kudriashov, T. Taniguchi, K. Watanabe, D. A. Svintsov, A. Principi, S. Adam, K. S. Novoselov, and D. A. Bandurin, "Anomalous terahertz photoconductivity caused by the superballistic flow of hydrodynamic electrons in graphene," arXiv:2403.18492 [cond-mat.mes-hall], 10.48550/arXiv.2403.18492 (2024).

[10] L. Wang, I. Meric, P. Y. Huang, Q. Gao, Y. Gao, H. Tran, T. Taniguchi, K. Watanabe, L. M. Campos, D. A. Muller, J. Guo, P. Kim, J. Hone, K. L. Shepard, and C. R. Dean, "One-Dimensional Electrical Contact to a Two-Dimensional Material," en, Science **342**, 614–617 (2013).

[11] F. D. Parmentier, L. N. Serkovic-Loli, P. Roulleau, and D. C. Glattli, "Photon-Assisted Shot Noise in Graphene in the Terahertz Range," Physical Review Letters **116**, 227401 (2016).

[12] COMSOL, *RF Module user's guide* (2023).

[13] S. Ramo, J. R. Whinnery, and T. Van Duzer, *Fields and Waves in Communication Electronics*, 3rd ed. (John Wiley & Sons, Nashville, TN, 1994-01).

[14] T. Udem, *Elektromagnetische Wellen und Optik*, lecture notes, Ludwig-Maximilians-Universität München, 2022.

[15] J. D. Jackson, *Classical Electrodynamics*, 3rd ed. (John Wiley & Sons, Nashville, TN, 1998-07).

[16] M. B. Steer, *Microwave and RF Design: Transmission Lines*, Vol. 2 (NC State University, 2019-07).

[17] M. B. Steer, *Microwave and RF Design: Networks*, Vol. 3 (NC State University, 2019-07).

[18] M. B. Steer, *Fundamentals of Microwave and RF Design* (NC State University, 2019-07).

[19] M. B. Steer, *Microwave and RF Design: Radio Systems*, Vol. 1 (NC State University, 2019-07).

[20] J. D. Kraus, *Antennas*, 2nd ed. (McGraw-Hill, New York, NY, 1988-04).

[21] P. J. Bevelacqua, Antenna-Theory.com, https://www.antenna-theory.com/ (visited on 2024-06-11).

[22] Wikimedia Commons, *Electromagnetic fields due to a radiating dipole*, (2012-09-12) https://commons.wikimedia.org/wiki/File:Felder_um_Dipol.svg (visited on 2024-06-13).

[23] R. Gonçalves Licursi De Mello, A. C. Lepage, and X. Begaud, "The bow-tie antenna: Performance limitations and improvements," IET Microwaves, Antennas & Propagation **16**, 283–294 (2022).

[24] R. Compton, R. McPhedran, Z. Popovic, G. Rebeiz, P. Tong, and D. Rutledge, "Bow-tie antennas on a dielectric half-space: Theory and experiment," IEEE Transactions on Antennas and Propagation **35**, 622–631 (1987).

[25] M. Bohman, N. Eivarsson, E. Grosfilley, and A. Lundberg, *Design and Simulation of Terahertz Antenna for Spintronic Applications*, 2020-06.

[26] Y. Wang, W. Jing, F. Han, Q. Meng, K. Yao, L. Zhao, Z. Jiang, and C. H. Chan, "Modified bow-tie antenna array with efficient electric near-field enhancement for terahertz band," Optics Communications **549**, 129849 (2023).

[27] D. Rutledge and M. Muha, "Imaging antenna arrays," IEEE Transactions on Antennas and Propagation **30**, 535–540 (1982).

[28] COMSOL, *COMSOL Multiphysics*, version 6.2.0.339, 2024.

[29] A. J. Jurschitzka, commissioned figure, 2024-06-27.

[30] W. Lv, J. Zhou, Y. Liu, and L. Xu, "Non-Euclidean conformal devices with continuously varying refractive-index profiles based on bispheres," Physical Review A **109**, 063506 (2024).

[31] D. H. Staelin, *Electromagnetics and Applications*, lecture notes, Massachusetts Institute of Technology, 2011.

[32] COMSOL, *COMSOL Multiphysics reference manual* (2023).

[33] M. Runge, D. Engel, M. Schneider, K. Reimann, M. Woerner, and T. Elsaesser, "Spatial distribution of electric-field enhancement across the gap of terahertz bow-tie antennas," Optics Express **28**, 24389 (2020).

[34] K. Shein, E. Zharkova, M. A. Kashchenko, A. I. Kolbatova, A. Lyubchak, L. Elesin, E. Nguyen, A. Semenov, I. Charaev, A. Schilling, G. N. Goltsman, K. S. Novoselov, I. Gayduchenko, and D. A. Bandurin, "Fundamental limits of few-layer $NbSe_2$ microbolometers at terahertz frequencies," Nano Letters **24**, 2282–2288 (2024).

[35] P. Maraghechi and A. Y. Elezzabi, "Experimental Confirmation of Design Techniques for Effective Bow-Tie Antenna Lengths at THz Frequencies," Journal of Infrared, Millimeter, and Terahertz Waves **32**, 897–901 (2011).

[36] M. Köfferlein, *KLayout*, version 0.29.2, 2024-06-08.

[37] H. Liu, J. Yu, P. Huggard, and B. Alderman, "A Multichannel THz Detector Using Integrated Bow-Tie Antennas," International Journal of Antennas and Propagation **2013**, 1–8 (2013).

[38] *PubChem compound summary for CID 180, Acetone*, in *PubChem* (National Center for Biotechnology Information, 2024).

[39] *PubChem compound summary for CID 3776, Isopropyl Alcohol*, in *PubChem* (National Center for Biotechnology Information, 2024).

[40] *PubChem compound summary for CID 13838, Hexamethyldisilazane*, in *PubChem* (National Center for Biotechnology Information, 2024).

[41] *AZ 5214 E photoresist data sheet* (Clariant AG).

[42] *AZ 326 MIF, AZ 726 MIF, AZ 826 MIF developer data sheet* (Clariant AG).

[43] R. C. Jones, "A New Calculus for the Treatment of Optical SystemsI Description and Discussion of the Calculus," Journal of the Optical Society of America **31**, 488 (1941).

[44] A. Altland and J. von Delft, *Mathematics for Physicists* (Cambridge University Press, 2019-02).

[45] *PubChem* (National Center for Biotechnology Information, 2024).

A Additional Derivations

A.1 Maxwell's Equations

A.1.1 Homogeneous Wave Equations

In the following, a homogeneous and linear medium is assumed. For the derivation of the solution of the homogeneous wave equations, it is necessary to take the curl of Eq. (2.10) and Eq. (2.13) in combination with the vector identity from Eq. (A.30). The calculations for the electric field are as follows [14, p. 8]:

$$\boldsymbol{\nabla} \times (\boldsymbol{\nabla} \times \mathbf{E}) = -\frac{\partial}{\partial t}(\boldsymbol{\nabla} \times \mathbf{B})$$

$$\boldsymbol{\nabla}(\underbrace{\boldsymbol{\nabla} \cdot \mathbf{E}}_{\text{Eq. (2.10)}}) - \boldsymbol{\nabla}^2 \mathbf{E} = -\mu \frac{\partial \mathbf{j}}{\partial t} - \varepsilon\mu \frac{\partial^2 \mathbf{E}}{\partial t^2} \tag{A.1}$$

$$\varepsilon\mu \frac{\partial^2 \mathbf{E}}{\partial t^2} - \boldsymbol{\nabla}^2 \mathbf{E} = -\mu \frac{\partial \mathbf{j}}{\partial t} - \boldsymbol{\nabla}\left(\frac{\rho}{\varepsilon}\right)$$

Analogous, for the magnetic flux one obtains:

$$\boldsymbol{\nabla} \times (\boldsymbol{\nabla} \times \mathbf{B}) = \mu(\boldsymbol{\nabla} \times \mathbf{j}) + \varepsilon\mu \frac{\partial}{\partial t}(\boldsymbol{\nabla} \times \mathbf{E})$$

$$\boldsymbol{\nabla}(\underbrace{\boldsymbol{\nabla} \cdot \mathbf{B}}_{\text{Eq. (2.11)}}) - \boldsymbol{\nabla}^2 \mathbf{B} = \mu(\boldsymbol{\nabla} \times \mathbf{j}) - \varepsilon\mu \frac{\partial^2 \mathbf{B}}{\partial t^2} \tag{A.2}$$

$$\varepsilon\mu \frac{\partial^2 \mathbf{B}}{\partial t^2} - \boldsymbol{\nabla}^2 \mathbf{B} = \mu(\boldsymbol{\nabla} \times \mathbf{j})$$

The obtained expressions are referred to as the inhomogeneous wave equations. In a charge and current free environment (explicitly, $\rho = 0$ and $\mathbf{j} = 0$), this equates to the well-known homogeneous wave equations [14, p. 8]:

$$\frac{n^2}{c^2}\frac{\partial^2 \mathbf{E}}{\partial t^2} - \boldsymbol{\nabla}^2 \mathbf{E} = 0 \qquad (\text{A.3}) \qquad\qquad \frac{n^2}{c^2}\frac{\partial^2 \mathbf{B}}{\partial t^2} - \boldsymbol{\nabla}^2 \mathbf{B} = 0 \qquad (\text{A.4})$$

Without further proof, the following relations for the speed of light in vacuum c and the refractive index n were used to obtain the final set of equations [14, pp. 8-9]:

$$c = \frac{1}{\sqrt{\varepsilon_0\mu_0}} \qquad (\text{A.5}) \qquad\qquad n = \sqrt{\epsilon_{\mathrm{r}}\mu_{\mathrm{r}}} \qquad (\text{A.6}) \qquad\qquad \frac{\omega}{|\mathbf{k}|} = \frac{c}{n} \qquad (\text{A.7})$$

The solution to these two differential equations can be calculated in numerous ways. For example, a fast approach would be to assume a solution with harmonic time dependence $e^{i\omega t}$ and then solve for the phasor (the spatial component) of the solution [15, p. 295][12, p. 83]. One of the many textbook solutions to both fields is (simplified) as follows, with the choice of the sign being arbitrary [14, p. 10]:

$$\mathbf{E}(t, \mathbf{x}) = \mathbf{E_0}e^{\pm i(\omega t - n\mathbf{k}\cdot\mathbf{x})} \qquad (\text{A.8}) \qquad\qquad \mathbf{B}(t, \mathbf{x}) = \mathbf{B_0}e^{\pm i(\omega t - n\mathbf{k}\cdot\mathbf{x})} \qquad (\text{A.9})$$

In this case, ω is the angular frequency, and $\mathbf{k}$ the angular wave vector of the wave in vacuum. $\mathbf{E_0}$ and $\mathbf{B_0}$ denote the Jones vectors of the plane wave, from which the magnitude and polarization of the fields can be inferred from [43]. This solution is referred to as the complex representation of a plane wave. It is important to emphasize that the actual physical fields are commonly defined as the real part of their complex representation, explicitly $\mathfrak{R}\{\mathbf{E}(t, \mathbf{x})\}$ and $\mathfrak{R}\{\mathbf{B}(t, \mathbf{x})\}$. The complex representation merely provides more convenience when employed in calculations. There are more solutions to this set

of equations other than the plane wave solution[11] discussed here and in Sec. 2, however, the plane wave solution suffices fully for the scope of this thesis. The calculated results for the electric and magnetic waves abide to some restrictions, but also give rise to new helpful relations accessible via further study of Maxwell's equations and their solution.

Explicitly, the resulting solutions are not independent from one another. Maxwell's equations still establish a relationship between $\mathbf{E}$ and $\mathbf{B}$, that must be fulfilled everywhere and at all times. For instance, when subjected to Maxwell's equations in free space and applying the vector identity Eq. (A.29), one arrives at the following restraints for the angular wave vector [14, p. 10]:

$$\boldsymbol{\nabla} \cdot \mathbf{E} = -in\mathbf{k} \cdot \mathbf{E} = 0 \qquad\qquad \Rightarrow \quad \mathbf{k} \perp \mathbf{E} \qquad\qquad (A.10)$$

$$\boldsymbol{\nabla} \cdot \mathbf{B} = -in\mathbf{k} \cdot \mathbf{B} = 0 \qquad\qquad \Rightarrow \quad \mathbf{k} \perp \mathbf{B} \qquad\qquad (A.11)$$

$$\boldsymbol{\nabla} \times \mathbf{E} = -in\mathbf{k} \times \mathbf{E} = -\frac{\partial \mathbf{B}}{\partial t} = -i\omega\mathbf{B} \qquad\qquad \Rightarrow \quad \mathbf{E} \perp \mathbf{B} \qquad\qquad (A.12)$$

The results imply in the case of a plane wave that $\mathbf{E}$, $\mathbf{B}$, and $\mathbf{k}$ form a set of right-handed orthogonal vectors. Therefore, it is not only possible to relate the direction of $\mathbf{B}$, given the direction of $\mathbf{E}$ and $\mathbf{k}$, but also the amplitude via the dispersion relation in Eq. (A.7):

$$|\mathbf{E_0}| = \frac{c}{n}|\mathbf{B_0}| \quad \Leftrightarrow \quad |\mathbf{B_0}| = \frac{n}{c}|\mathbf{E_0}| \qquad (A.13) \qquad \mathbf{E_0} \times \mathbf{B_0} = \frac{n}{c}|\mathbf{E_0}|^2\frac{\mathbf{k}}{|\mathbf{k}|} = \frac{|\mathbf{E_0}|^2}{\omega}\mathbf{k} \qquad (A.14)$$

Conveniently, this allows to infer the magnetic flux from the electric field and vice versa in the scenario of a plane wave.

A.1.2 Poynting Theorem

Another practical observation regarding Maxwell's equations is the so-called Poynting theorem, which relates the electromagnetic fields to power transport. Amongst other results, the theorem yields the Poynting vector, which represents the direction and magnitude of energy flux. To allow for easier calculations with the complex representation of the plane wave solution, the complex Poynting theorem will be utilized instead. The theorem is derived via the vector identity in Eq. (A.31) and Maxwell's equations Eq. (2.3) and Eq. (2.4) [15, sec. 6.9][31, eqs. 2.7.5, 2.7.21–2.7.22]:

$$-\boldsymbol{\nabla} \cdot (\mathbf{E} \times \mathbf{H}^*) = \mathbf{E} \cdot (\boldsymbol{\nabla} \times \mathbf{H}^*) - \mathbf{H}^* \cdot (\boldsymbol{\nabla} \times \mathbf{E})$$
$$= \mathbf{E} \cdot \mathbf{j}^* + \mathbf{E} \cdot \frac{\partial \mathbf{D}^*}{\partial t} + \mathbf{H}^* \cdot \frac{\partial \mathbf{B}}{\partial t}$$
$$\Updownarrow \qquad\qquad\qquad\qquad\qquad (A.15)$$
$$\Leftrightarrow \quad 0 = \boldsymbol{\nabla} \cdot \underbrace{(\mathbf{E} \times \mathbf{H}^*)}_{\text{(I)–(II)}} + \underbrace{\mathbf{E} \cdot \mathbf{j}^*}_{\text{(III)}} + \underbrace{\mathbf{E} \cdot \frac{\partial \mathbf{D}^*}{\partial t}}_{\text{(IV)}} + \underbrace{\mathbf{H}^* \cdot \frac{\partial \mathbf{B}}{\partial t}}_{\text{(V)}}$$

The real physical quantities derived from the Poynting theorem, including the intensity I, mostly take only the real part of $\mathbf{S}$ into account. Summarized [15, p. 259][31, sec. 2.7]:

(I)	Poynting vector	$\mathbf{S} = \mathbf{E} \times \mathbf{H}^*$	(A.16)
(II)	Intensity	$I = |\mathfrak{R}\{\mathbf{S}\}|$	(A.17)
(III)	Joule heating	$P_{\text{joule}} = \mathbf{E} \cdot \mathbf{j}^*$	(A.18)

---

[11]Other solutions, for instance, are the spherical wave solution or (more related to optics) the solutions for various beam shapes (such as Gaussian- or Bessel-shaped beams).

(IV)   Electric energy density $w_{\mathrm{e}} = \dfrac{1}{2}\varepsilon|\mathbf{E}|^2$ (A.19)

(V)   Magnetic energy density $w_{\mathrm{m}} = \dfrac{1}{2}\mu|\mathbf{B}|^2$ (A.20)

Any time-averaged quantities of varying fields with harmonic time dependence derived from the Poynting vector (II) – (V) and the Poynting vector itself (I) must be multiplied by a factor of 1/2 to account for the instantaneously varying fields [15, p. 264], explicitly:

$$\langle\mathbf{S}\rangle_T = \frac{1}{2}\mathbf{S} \qquad\text{(A.21)} \qquad\qquad \langle I\rangle_T = \frac{1}{2}I \qquad\text{(A.22)}$$

and so on.

For the plane wave solution obtained in Eq. (A.8) and Eq. (A.9), without any component traveling in the reverse direction and by applying the third constitutive relation for the current density from Eq. (2.7) and in combination with the equation for Joule heating, one obtains:

$$\mathbf{S} = \sqrt{\frac{\varepsilon}{\mu}}|\mathbf{E_0}|^2\frac{\mathbf{k}}{|\mathbf{k}|} = cn\frac{\varepsilon_0}{\mu_{\mathrm{r}}}|\mathbf{E_0}|^2\frac{\mathbf{k}}{|\mathbf{k}|} \quad\text{(A.23)} \qquad P_{\mathrm{joule}} = \sigma|\mathbf{E_0}|^2 \quad\text{(A.26)}$$

$$|\mathfrak{R}\{\mathbf{S}\}| = cn\frac{\varepsilon_0}{\mu_{\mathrm{r}}}|\mathbf{E_0}|^2 \quad\text{(A.24)} \qquad w_{\mathrm{e}} = \frac{1}{2}\varepsilon|\mathbf{E_0}|^2 \quad\text{(A.27)}$$

$$|\mathfrak{I}\{\mathbf{S}\}| = 0 \quad\text{(A.25)} \qquad w_{\mathrm{m}} = \frac{1}{2}\mu|\mathbf{B_0}|^2 \quad\text{(A.28)}$$

A.2 Vector Calculus Identities

The following vector calculus identities have been taken from Altland et al. [44, sec. V3.7] and are listed for the sake of completeness. Here, $\mathbf{a}$ and $\mathbf{b}$ denote vector fields.

[44, eq. V115b] $\boldsymbol{\nabla}\cdot(\boldsymbol{\nabla}\times\mathbf{a}) = 0$ (A.29)

[44, eq. V115c] $\boldsymbol{\nabla}\times(\boldsymbol{\nabla}\times\mathbf{a}) = \boldsymbol{\nabla}\cdot(\boldsymbol{\nabla}\mathbf{a}) - \boldsymbol{\nabla}^2\mathbf{a}$ (A.30)

[44, eq. V116d] $\boldsymbol{\nabla}\cdot(\mathbf{a}\times\mathbf{b}) = \mathbf{b}\cdot(\boldsymbol{\nabla}\times\mathbf{a}) - \mathbf{a}\cdot(\boldsymbol{\nabla}\times\mathbf{b})$ (A.31)

Affidativ

I hereby declare that this thesis is my own work, and that I have not used any sources and aids other than those stated in the thesis.

Hiermit erkläre ich, die vorliegende Arbeit selbständig verfasst zu haben und keine anderen als die in der Arbeit angegebenen Quellen und Hilfsmittel benutzt zu haben.

Munich, July 22, 2024
München, 22. Juli 2024

—————————————————————

Carl Artemus Hudeczek